Summer 8-13-2022

ASSESSING THE RISK OF LAND SUBSIDENCE IN THE LOWER LIMPOPO RIVER BASIN, MOZAMBIQUE WITH REMOTE SENSING

Gabriella Zuccolotto

ASSESSING THE RISK OF LAND SUBSIDENCE IN THE LOWER LIMPOPO RIVER BASIN, MOZAMBIQUE WITH REMOTE SENSING

A Thesis

Submitted to the Bayer School of Natural and Environmental Sciences

Duquesne University

In partial fulfillment of the requirements for

the degree of Master of Science

By

Gabriella Zuccolotto

August 2022

ASSESSING THE RISK OF LAND SUBSIDENCE IN THE LOWER LIMPOPO RIVER BASIN, MOZAMBIQUE WITH REMOTE SENSING

By

Gabriella Zuccolotto

Approved 30 June 2022

David M. Kahler Professor of Environmental Science (Committee Chair)	Theodore Corcovilos Professor of Physics (Committee Member)
Philip Reeder Professor of Environmental Science (Committee Member)	
Ellen Gawalt Dean, Bayer School of Natural and Environmental Sciences	John F. Stolz Director, Center for Environmental Research and Education

ABSTRACT

ASSESSING THE RISK OF LAND SUBSIDENCE IN THE LOWER LIMPOPO RIVER BASIN, MOZAMBIQUE WITH REMOTE SENSING

By

Gabriella Zuccolotto

August 2022

Dissertation supervised by Professor David M. Kahler.

Land subsidence is a threat to coastal cities around the world. In the lower Limpopo River Basin, the presence of compaction-prone alluvial sediments, groundwater use, and reports of saltwater intrusion suggest that subsidence could be occurring. Using interferometric synthetic aperture radar (InSAR) from Sentinel-1, combined with in-situ sea level and river height measurements, this study aims to determine if land subsidence could contribute to increased saltwater intrusion. InSAR results indicate that subsidence in the lower Limpopo River valley has occurred at an average rate of -2.98 cm/yr based on data from the dry seasons (May to October) of 2017-2021. River height is decreasing at a rate of -1.93 cm/yr and sea level is rising at 0.114 cm/yr. Given the detected rate of land subsidence, this presents a novel risk for relative sea level rise and likely contributes to the increased salinization of the lower Limpopo River.

ACKNOWLEDGEMENT

I would like to thank Duquesne University, the Center for Environmental Research and Education, and the rest of the Limpopo Resilience Lab for supporting this research and providing me with the knowledge and skills necessary to excel in this field. I would also like to thank the U.S. Agency for International Development for funding this work, as well as the Alaska Satellite Facility, ESA Copernicus mission, Mozambique Regional Administration of Waters in the South (ARA-SUL) and University of Hawaii Sea Level Center for supplying data for this project.

Thank you to my thesis committee members, Dr. Ted Corcovilos and Dr. Philip Reeder, as well as my research advisor, Dr. David Kahler, for their time and guidance. Dr. Kahler, working in your research lab has been a wonderful experience, and I am grateful for the kindness, patience, and knowledge you have showed me over the past two years. As your advisee, I have grown my skill set and gained confidence as a researcher. Remember when I told you I was scared of doing a computational thesis project?

I would also like to thank Dr. Steve Hovan and the IUP Geology Department for believing in my capabilities as both a scientist and educator. My time in the department has greatly contributed to my success in graduate school, and I am proud to be an IUP alumni.

Finally, I would like to acknowledge my family and friends for their encouragement throughout this process. To my parents, thank you for being my biggest supporters and instilling in me a strong work ethic and love for science. When you told me to “train my brain” every morning before I left for school, did you think this would be the outcome? Thank you to my sisters for your unwavering support and reassurance. To my grandparents, aunts, uncles, cousins, friends, former students, and all those that I love, thank you for motivating me.

TABLE OF CONTENTS

LIST OF FIGURES

CHAPTER 1: INTRODUCTION

Land subsidence, defined as the sinking of the Earth's surface due to the displacement of subsurface materials, has been observed in coastal cities around the world (Wu et al., 2022). Subsidence frequently occurs in coastal, depositional environments, such as floodplains and river deltas, and can have detrimental environmental and economic consequences for coastal communities (Bagheri-Gavkosh, 2021). Many cities are subsiding at a faster rate than sea level is rising, which can result in increased flooding and land loss from permanent inundation of seawater, saltwater intrusion into surface and groundwater sources and infrastructure damage (Erkens et al., 2015; Higgins, 2015). The impacts of land subsidence are far-reaching with over 339 million people living in subsidence-prone, deltaic environments in 2017 (Edmonds et al., 2021). A 2021 study published in Science found that by 2040, 19% of the world's population may be threatened by land subsidence (Herrera-García et al., 2020).

1.1 MECHANICS OF LAND SUBSIDENCE

Many densely populated coastal cities, such as Jakarta (Indonesia), Bangkok (Thailand), and New Orleans (United States), were built on alluvium, or unconsolidated sand, silt, and clay sediments that were eroded and subsequently deposited by rivers (Higgins, 2015). Alluvial environments, such as floodplains and river deltas, have been developed by humans due to their natural availability of freshwater and nutrient-rich soils for agriculture (Stanley & Warne, 1997). These sediments are highly vulnerable to subsidence, due to the soft, compressible nature of unconsolidated alluvium deposits (Törnqvist et al., 2008; Stanley & Clemente, 2014). Natural compaction occurs as the weight of newly deposited sediments exerts pressure on the underlying layers, forcing water out of pore spaces in saturated soils and reducing void space in unsaturated soils (Higgins, 2015). Susceptibility to natural compaction is influenced by the thickness of

overlying layers and sediment grain size, with coarse grained sediments, such as gravel and sand, exhibiting less compaction than fine-grained sediment, such as silt and clay. Additionally, sediments that contain high levels of organic matter, such as peat, are more susceptible to subsidence due to the release of carbon dioxide during oxidation (Hoyt et al., 2020). For example, the draining of farmland in the Po Delta in Italy between 1892 and 1967 has resulted in peat oxidation and subsequent subsidence of 2 meters (Gambolati et al., 2006).

Land subsidence can occur naturally in alluvial environments; however, this process can be and is often accelerated by anthropogenic activity (Syvitski et al., 2009; Galloway et al., 2016). Groundwater extraction for irrigation of crops, industrial activity, and domestic consumption is the leading cause of human-induced land subsidence around the world (Galloway & Burbey, 2011; Higgins, 2015). As groundwater is pumped from the subsurface, the water table lowers and pore spaces collapse, resulting in subsidence at the surface and reduction of the aquifer's storage capacity (Gambolati & Teatini, 2015). If the rate of extraction continually exceeds the rate of recharge, permanent aquifer compaction can occur (Haghshenas & Motagh, 2019). The relationship between groundwater extraction land subsidence has been documented around the world (Herrera-García et al., 2020). For example, Bell et al (2008) used interferometric synthetic aperture radar (InSAR) measurements and borehole data from extensometers to demonstrate the relationship between groundwater extraction and land subsidence in Las Vegas Valley, Nevada. Similarly, Liu et al (2019) used Sentinel-1 InSAR and GPS measurements, as well as GRACE-derived groundwater anomaly measurements to show correlation between the over-abstraction of groundwater for crop irrigation and subsidence in California's Central Valley.

The construction of dams, levees and embankments can also contribute to land subsidence by reducing deposition of sediment loads downstream (Syvitski et al., 2005). In natural settings, sediments deposited by the river build up the delta as it subsides, keeping the system in a state of equilibrium. When the sediment supply is cut off by hydrologic infrastructure, replenishment cannot occur and the rate of subsidence increases, as has been observed in the Mekong and Nile River deltas (Kondolf, Rubin & Minear, 2014; Becker & Sultan, 2009). Syvitski et al (2009) analyzed 33 river deltas and found that 28 were experiencing reduced sediment deposition and 11 were experiencing virtually no deposition and/or very accelerated compaction. Edmonds et al (2021) found the effects of reduced aggradation to be widespread with 25 million people residing on sediment-starved deltas in 2017.

Additionally, the overlying weight of infrastructure can exacerbate subsurface compaction. Parsons (2021) and Yang et al (2018) found that building loads have caused localized land settling in the San Francisco Bay area and Eastern Beijing, respectively. The contribution of infrastructure weight should be included in quantifications of land subsidence as urbanization continues in the future. The 2018 Revision of World Urbanization Projects found that 55% of the global population lives in urban areas and that this number will increase to 68% by 2050 (United Nations, 2019).

1.2 CONSEQUENCES OF LAND SUBSIDENCE

Land subsidence in coastal environments increases the rate of relative sea level rise (RSLR) and exacerbates flood risk (i.e. flood duration, extent and frequency). Syvitski et al (2009) found that, out of 33 major river deltas, 85% experienced significant flooding, which led to the temporary submergence of 260,000 km^2 of land. They estimate that the area of deltas at risk for flooding could increase by 50% under sea-level rise (SLR) estimates for the 21st century.

Megacities in Asian, such as Tokyo, Jakarta, and Ho Chi Minh City, were constructed on deltaic sediments and experience some of the fastest rates of subsidence in the world (Erkens et al., 2015). Due to the significant flooding that these cities experience, adaptation measures, such as groundwater pumping regulation and the relocation of Indonesia's capital (Jakarta) have already been established to combat the effects of subsidence (Cao et al., 2021). Subsidence-induced flooding has the potential to displace millions of people, particularly those that already experience from flooding from tropical cyclone activity and storm surges. Edmonds et al (2021) found that in 2017 there were 339 million people living on river deltas, with 89% lying in zones of tropical cyclone activity.

Coastal land subsidence increases the hydraulic pressure of seawater which, in turn, can increase saltwater intrusion into fresh surface and groundwater sources. In natural, coastal systems freshwater and saltwater mix at an interface known as the zone of dispersion This boundary exists in a state of equilibrium near the coast and deep below the land surface. However, anthropogenic activity, such as groundwater extraction and diminished surface flows, can reduce the seaward movement of freshwater, disturbing the equilibrium and allowing saltwater to move further in-land (Xiao et al., 2021; Antonellini et al., 2008). This allows for easier saltwater encroachment, particularly during tropical cyclone storm surges and high tides (Xiao et al., 2021). Subsidence increases contamination of groundwater wells and surface water bodies with saltwater, rendering them unusable for drinking and crop irrigation (Schmidt, 2015). Salinization can have steep economic consequences for coastal communities that rely heavily on agriculture.

Subsidence can also damage civil infrastructure, such as buildings, bridges, and roads. Li et al (2021) found that groundwater extraction has caused land subsidence and differential

settling of the Nanpu Bridge in Shanghai. In urban areas of Indonesia, land subsidence has resulted in cracking roads, “sinking” houses, lowering of bridge structures and disruptions to water drainage systems (Abidin et al., 2015).

1.3 MEASURING LAND SUBSIDENCE

A variety of airborne and ground-based techniques have been used to measure land subsidence (Galloway & Burbey, 2011). Prior to the 1980s ground-based techniques for subsidence monitoring were used, including optical leveling and extensometers. However, these techniques are time-consuming and labor intensive. The evolution of global position system (GPS) in the 1980s revolutionized spaceborne subsidence detection. Today, spaceborne synthetic aperture radar (SAR) is becoming a leading method for global land subsidence monitoring. Current SAR satellites in orbit include the Canadian Space Agency’s RADARSAT-2, the German Aerospace Center’s TerraSAR-X and the European Space Agency’s Sentinel-1.

Synthetic aperture radar (SAR) is an active imaging sensor, meaning that it produces its own energy rather than collecting reflected energy emitted by an exterior source (Jansing, 2021). Traditionally, the spatial resolution of radar is limited by the ratio of the sensor’s wavelength to the antenna length. Because large antennas are not practical for spaceborne radars, synthetic apertures have been developed. These radars use the Doppler shift detected by a series of pulses taken in quick succession to simulate a larger antenna and increase spatial resolution. Different SAR satellites operate in a range of wavelengths, such as X-band ($\lambda = 3.1$ cm), C-band ($\lambda = 5.6$ cm) and L-band ($\lambda = 23$ cm). The band of the radar controls the surface properties that the satellite can successfully monitor. For example, C-band radar can monitor low-lying vegetation while L-band, which has a greater wavelength, can penetrate deeper into dense vegetation and forests.

As a spaceborne SAR orbits Earth, it emits pulses of electromagnetic radiation which reflect off the Earth's surface and return to the satellite, recording the phase and amplitude of the return signal (Jansing, 2021). Phase measurements, which are fractions of a complete sine wave cycle, determine the distance between the sensor and surface, while amplitude measures the strength of the backscattered wave and yields information about the properties of the surface, such as the roughness and dielectric constant. SAR can be used to measure land deformation over time using a technique called interferometric SAR, or InSAR. InSAR is a repeat-pass remote sensing technique that records shifts in phase between two SAR images, displayed as maps called interferograms.

Advantages of the InSAR technique include the detection movement with high precision, down to the mm scale and at large spatial and temporal scales. Spaceborne SAR allows for continuous global coverage of the Earth's surface, day and night, regardless of cloud cover. It also allows for monitoring of areas that are potentially dangerous or difficult to reach. Modern-day SAR satellites, such as Sentinel-1, have exceptional orbital stability and high temporal resolution due to frequent repeat cycles. Additionally, data collected by commercial SAR satellites is often publicly accessible and free. This technique can be used to observe for a wide range of applications, including crustal deformation from earthquakes and volcanic activity, landslides, and subsidence caused by aquifer compaction (Schlogel et al., 2015; Hooper et al., 2007; Jónsson et al., 2002; Galloway et al., 1998).

Limitations to the InSAR technique include variations in coherence of the interferometric pairs (Klees & Massonnet, 1998). Coherence, which can be both spatial and temporal in nature, is a measurement of similarity of the radar response between two SAR images and is controlled by properties of ground cover. Coherence values are high in areas where ground cover remains

the same over time, such as cities, bare rock exposures and deserts. Low coherence occurs in agricultural and vegetated areas, as well as areas of high snowfall and bodies of water, due to the significant changes in land cover that occur between the images. For this same reason, coherence degrades over increasingly long temporal scales. Choosing images with short temporal baselines between them can help to reduce this decorrelation. Coherence corresponds to the validity of the InSAR results, and therefore, areas of low coherence values should be ignored when interpreting findings.

Another limitation to InSAR is that, without the inclusion of additional data, it can only be used to measure relative displacement. Phase shifts are only resolvable relative to another point in the image. To be able to assume absolute deformation, you must compare phase shifts to an area in the interferogram that experiences no deformation, known as a reference pixel. Reference pixels can be determined using ground controls (GPS or similar) to determine stability at specific points.

1.4 STUDY AREA: THE LOWER LIMPOPO RIVER BASIN

The Limpopo River basin (LRB), located in semi-arid southern Africa, is a complex, transboundary system with a total drainage area of 408,250 km^2, distributed across South Africa (45%), Zimbabwe (15%), Botswana (20%) and Mozambique (20%) (LBPTC, 2010). The headwaters of the Limpopo rise in South Africa, where the river then flows in an eastward path along the borders of Botswana and Zimbabwe, through southern Mozambique, and eventually into the Indian Ocean near the coastal city of Xai-Xai, traveling a total length of 1,770 km (Figure 1). The Limpopo River has one major tributary, the Olifants River, along with smaller, intermittent tributaries. It is an essential source of freshwater for over 18 million people across 27 sub-basins (LIMCOM, 2013).

Climate and topography vary considerably across the LRB (LBPTC, 2010). Climatic zones range from tropical dry deserts and savannahs in the interior of the basin to tropical, rainy along Mozambique's coastal plain. Highest elevations (>2,000 m) occur in the Waterberg, Strydpoort Mountains and Drakensberg Range of South Africa and lowest elevations occur in the floodplains of southern Mozambique, where the final 175 km of the Limpopo River is situated below 7 meters above sea level (Figure 1). Mean annual precipitation (MAP) of the LRB is 530 mm/yr, ranging from 200 mm/yr to 1,200 mm/yr.

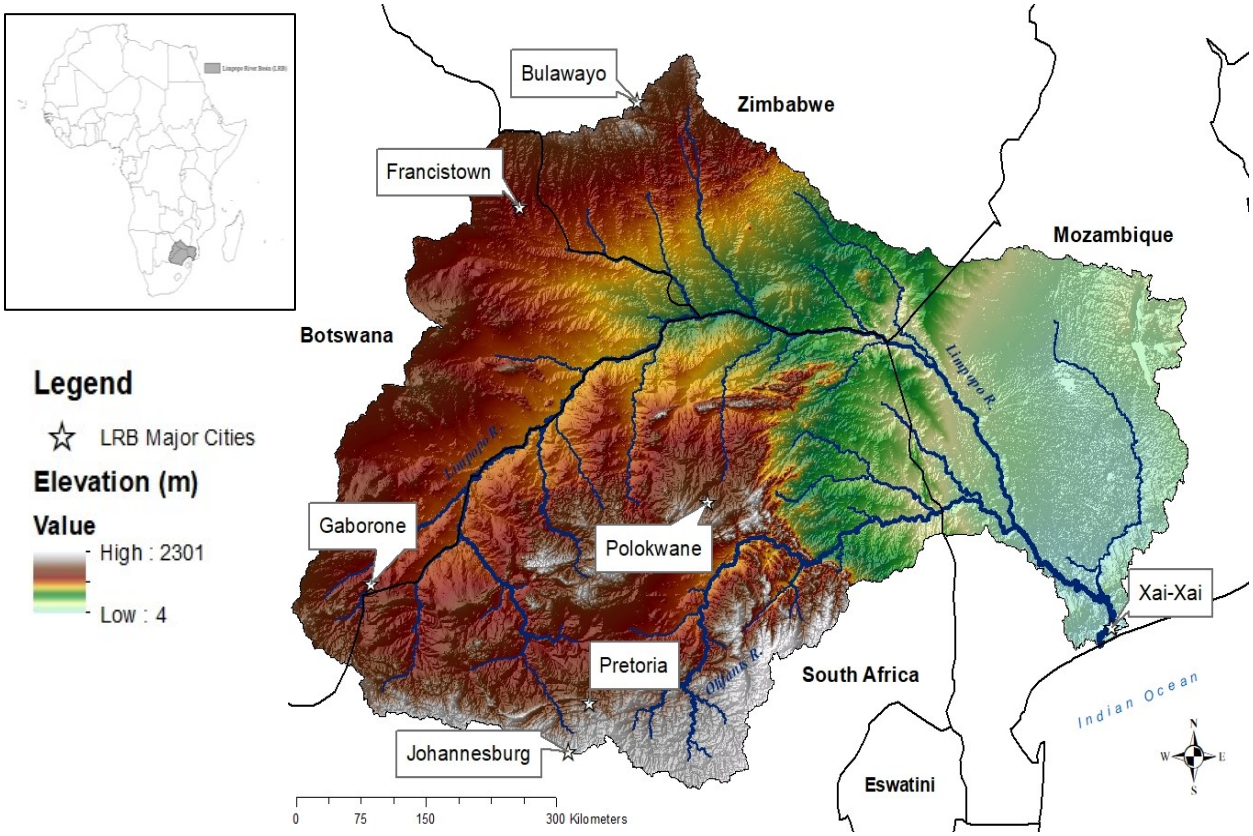

Figure 1: Geography of the Limpopo River Basin in southern Africa.
Data Source: Shuttle Radar Topography Mission (SRTM), 2013

Rainfall generally decreases from east to west and north to south across the basin, with exception of the mountainous region of South Africa, where the orographic effect generates pockets of high precipitation (Mosase & Ahiablame, 2018). High precipitation also occurs in the

lower Limpopo basin, located along the coast of southern Mozambique. Latitudinal movement of the Inter-Tropical Convergence Zone (ITCZ) controls temporal rainfall patterns, producing a cool, rainy season from November to April and hot, dry season from May to October (FAO, 2004). Approximately 95% of precipitation in the basin occurs between October and April. Interannual rainfall trends are also highly variable due to influence by El Niño–Southern Oscillation (ENSO) events that bring severe droughts and intense rainy periods and flooding to the LRB.

The Limpopo River Basin is home to some of southern Africa's most important agricultural areas and urban/industrial centers, as well as an abundance of mineral resources (LIMCOM, 2013). Major uses of water in the basin include crop irrigation, which accounts for 50% (2,415 x 10^6 m^3/yr) of total water demand, along with urban supply for major cities such as Gaborone and Francistown (Botswana), Pretoria, Johannesburg, and Polokwane (South Africa), Bulawayo and Beitbridge (Zimbabwe) and Xai-Xai and Chokwè (Mozambique) (LBPTC, 2010). In rural communities, water is used for domestic supply, livestock watering and crop irrigation. As a semi-arid, transboundary basin with high water demand, erratic rainfall, and frequent droughts, the LRB is plagued by physical water scarcity (Hoekstra et al., 2012; Petrie et al., 2015). Water scarcity occurs when water demand exceeds availability and is the greatest threat to the livelihood, economy, and environment of the LRB. Water scarcity also means that there is little water left for further development of the basin (Ashton & Hardwick, 2008).

Water governance in transboundary basins is complex and can potentially lead to conflict among riparian states (Ashton & Hardwick, 2008). To limit conflict and promote access to clean, freshwater for all that reside in the LRB, a transboundary water management (TWM) approach has been implemented. Multiple regional and local organizations and agreements have been

established to guide the equitable distribution of water resources in the LRB. All four countries in the LRB are members of the Southern African Development Community (SADC), which was established in 1980 to promote sustainable and equitable economic growth and socio-economic development in the countries of southern Africa. SADC's Protocol on Shared Watercourses, which was last revised in 2000, provides guidance for TWM in southern Africa (LIMCOM, 2013). Additionally, multiple local collaborations have been established among the riparian states, such as the Limpopo Basin Permanent Technical Committee (LBPTC) in 1986 and Limpopo Watercourse Commission (LIMCOM) in 2003 (LBPTC, 2010; LIMCOM, 2013). Effective TWM and water use agreements established by these organizations are essential for conserving water quantity and quality, particularly for those in downstream communities, such as those in the lower Limpopo River Basin of Mozambique.

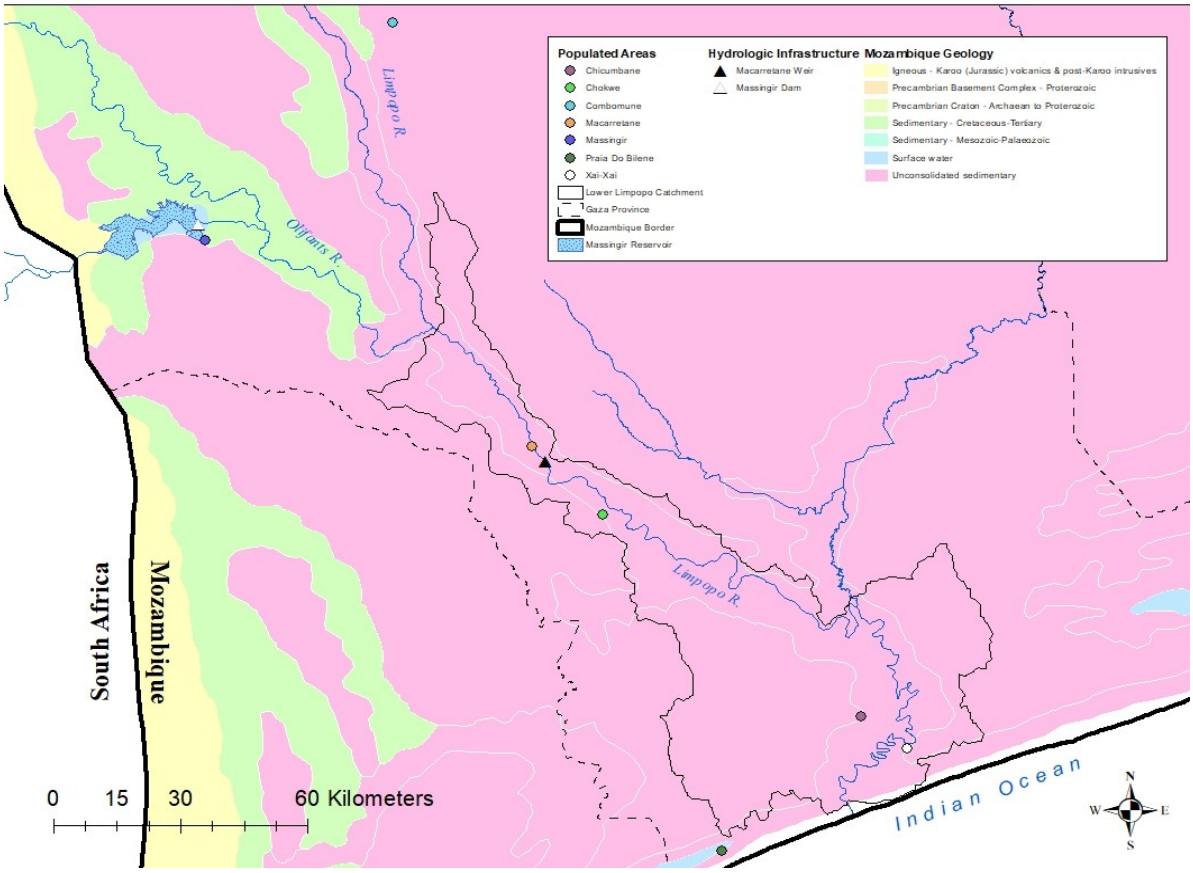

Figure 2: Geology of the lower Limpopo River basin with major population centers and hydrologic infrastructure.

The lower Limpopo River basin (LLRB) extends from the confluence of the Limpopo and Olifants River in Mozambique to the mouth of the Limpopo River, near the port town of Xai-Xai. The LLRB is a coastal plain landscape that drains an area of approximately 5,075 km^2 and is underlain by unconsolidated alluvium, composed of Quaternary-aged sand and gravel, as well as silt, mud, and clay (FAO, 2004; LIMCOM, 2013) (Figure 2). It is a low-lying catchment, with a maximum elevation of 157 meters above sea level and is dominated by the Limpopo River floodplain (Figure 3). Soils in the LLRB are mainly composed of fluvisols, or young soils in alluvial deposits that are usually found on level topography that is periodically flooded, such as in river floodplains and deltas and in coastal lowlands. (FAO, 2004).

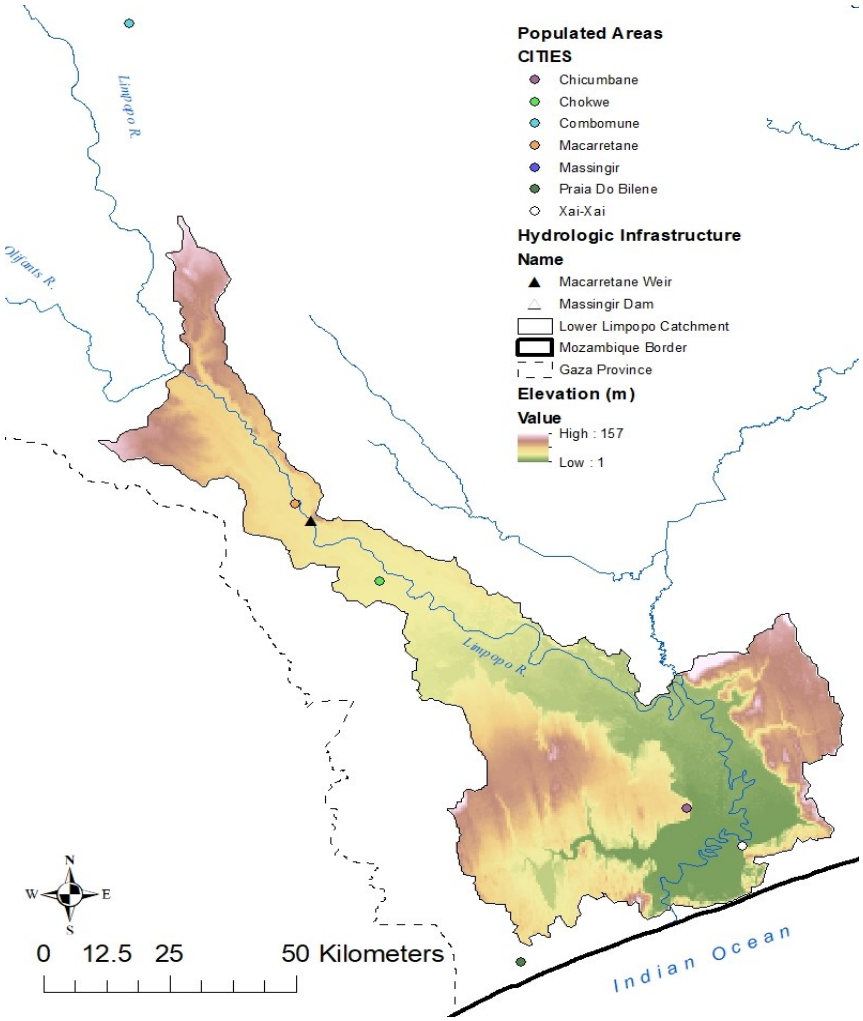

Figure 3: Topography of the lower Limpopo River Basin.
Data Source: SRTM, 2013

Water enters the LLRB through two rivers: the Limpopo (main stem) and Olifants. Flow from the Olifants branch is controlled by Massingir Dam. Massingir Dam, located on the Olifants River, has the largest storage capacity (2,800 x 10^6 m^3) of any dam in the LRB and is the second largest dam in Mozambique. The Changane River is a smaller tributary which also flows into the LLRB; however, this river flows intermittently and does not possess any major reservoirs that allow water to be stored for the dry season. Because the Changane River contributes little to overall water supply in the LLRB, the tributary will be disregarded in this study. Besides river flow entering the sub-basin, the LLRB also receives an average of 750-800 mm of rainfall per year (LBPTC, 2010). This rate varies interannually based on tropical cyclone and drought events. Past the confluence of the Limpopo and Olifants, the river continues southward eventually flowing through the Macarretane Weir. This dam has a smaller storage capacity of 4 x 10^6 m^3 and is used for irrigation supply to the downstream Chokwe Irrigation Scheme (CIS) (LBPTC, 2010). South of the CIS, the river valley is dominated by crop production from larger schemes and small hold farms (Figure 4). Eventually the river flows to the port town of Xai-Xai, which is the largest population in the LLRB and is home to approximately 130,000 people. Extensive agricultural schemes exist around Xai-Xai as well.

In the lowermost section of the LLRB, the river flows into the Indian Ocean, forming the Limpopo River estuary. Estuaries form an interface between the river and ocean and are therefore brackish in nature and tidally influenced. The Limpopo estuary passes through the dune-field that protects the coast and stretches approximately 35 km upstream, with mangrove communities bordering the river on both banks for the first 20 km (LIMCOM, 2013). Mangroves, which are tolerant to high salt concentrations, help to prevent erosion and absorb impacts from storms entering the LLRB from the Indian Ocean.

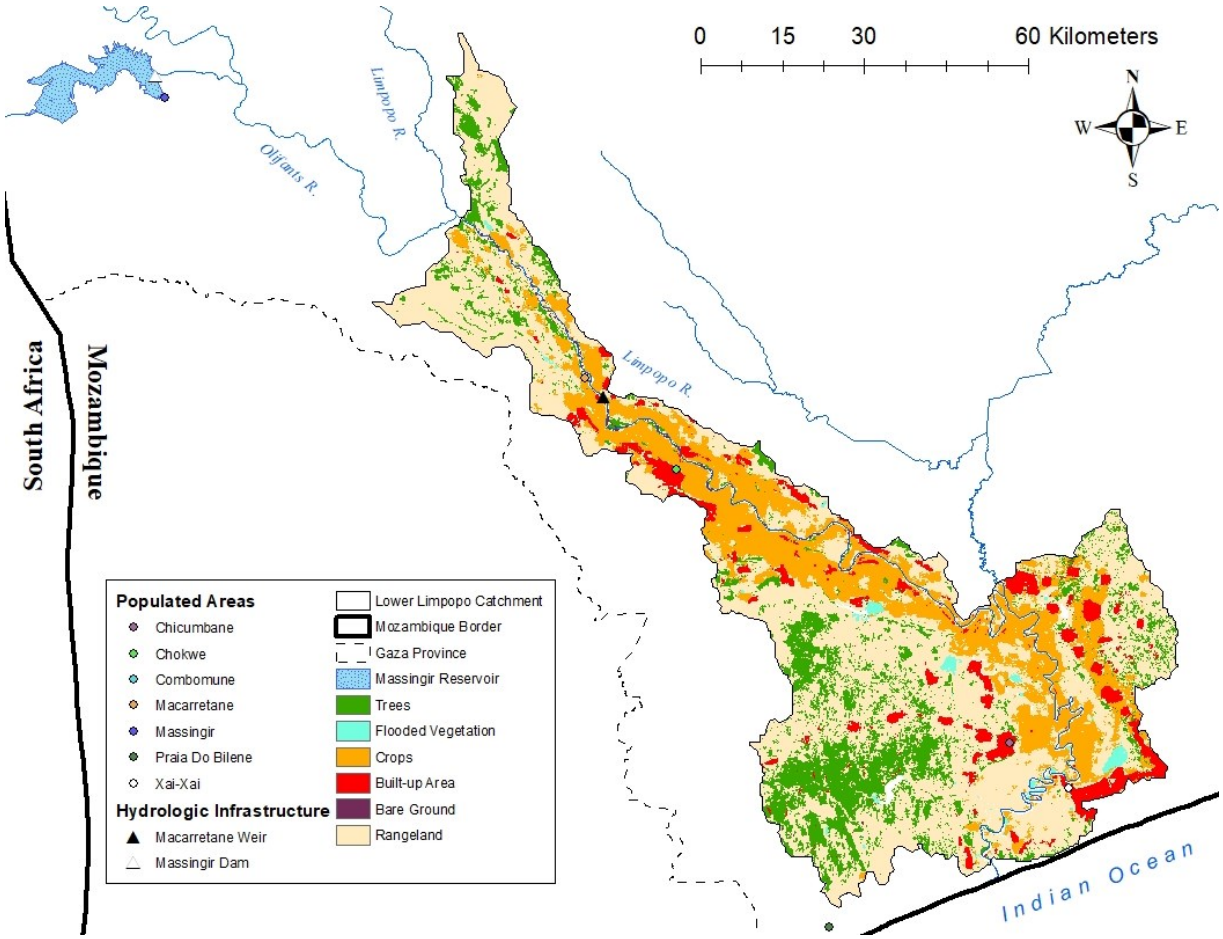

Figure 4: Land use in the lower Limpopo River Basin.
Data Source: Karra et al., 2021

1.4.1 AGRICULTURE

Agriculture is the dominant economic sector in Mozambique. It is responsible for 20% of the country's GDP and employs 80% of the country's workforce, 60% of which are women (FAO, 2005). Family-run farms, also referred to as smallholder farms, are vital to the success of this sector, as they account for 95% of the land area under production. In 2018, Mozambique was responsible for the production of 8.5 million tons of cassava, 3 million tons of sugarcane and 1.6 million tons of maize (FAO, 2018). Cotton, cashew nuts, sugar cane, tobacco and tea are all major export crops of Mozambique.

The lower Limpopo River valley is one of Mozambique's most productive agricultural hubs due to presence of nutrient-rich alluvium and access to freshwater. Land cover in the valley is dominated by a combination of large agricultural schemes and smallholder farms, as indicated by the orange areas in Figure 4. The Chokwe Irrigation Scheme (CIS), located in the Chokwe District of the LLRB, runs for 50 km along both banks of the Limpopo River and is the largest irrigation scheme in Mozambique with an area of 33,000 ha (Ismael et al, 2021). Commonly grown crops in the LLRB include maize, rice, cabbage, lettuce, tomatoes, sorghum, cowpeas, bananas and sweet potatoes. Many of the smallholder farms in the Limpopo River valley are subsistence farmers that primarily grow rice, but also grow an assortment of other vegetables and raise livestock to protect themselves against food scarcity. Rice is typically grown on wetlands over a single rainy season (October-March) and then replaced with vegetables during the dry season.

Rice production in the LLRB has grown over the past few decades in attempt to close the 300,000 ton/yr rice deficit that the country experiences (Ismael et al, 2021). This deficit has been largely attributed to lack of support for smallholder and (<5 ha) and medium holder (5-20 ha) farms, who are major producers of rice in the area, insufficient access to farming resources like fertilizer and mechanical equipment, and insufficient supply of water for irrigation. Mozambique has had to rely on imports from Asian countries to supplement their rice production.

1.4.2 WATER USE

Almost all water demand in the Mozambique portion of the LRB (270×10^6 m^3/yr) is used for crop irrigation (LBPTC, 2010). Larger, state-owned agricultural projects are irrigated by drainage channels that divert water out of the Limpopo River. Smallhold farmers depend more heavily on rainfall and groundwater extraction for crop irrigation. Groundwater is also used for

domestic supply in many rural communities, accounting for 9 x 10^6 m^3/yr of water demand. Highly productive shallow aquifers exist near the river as they recharge quickly. However, these aquifers are at risk of saltwater contamination by over-abstraction. Little is known about how much water is currently being exploited by the numerous small-scale users of surface and shallow, alluvial groundwater.

Urban and industrial demand (4 x 10^6 m^3/yr) are minor compared to agricultural demand (LBPTC, 2010). Xai-Xai and Chokwe's municipal water supply comes from groundwater extraction. Groundwater at Xai-Xai comes from the highly productivity coastal dune system that borders the Mozambique coast. Groundwater wells produces water at a rate of approximately 5 to 10 m^3/h per km^2 in this aquifer. However, like groundwater from within the river valley, there is little knowledge of where, when, and how much groundwater is being used in the Xai-Xai dune system.

1.4.3 THREATS TO WATER SECURITY

Water and food security threatened in the LLRB. Severe floods have occurred in the lower Limpopo catchment due to an influx of precipitation during tropical cyclone events, entering the basin from the Indian Ocean. For example, in February of 2000, Cyclone Eline devastated the lower reach of the Limpopo Basin, resulting in more than 700,000 displaced people, 1,000 deaths, and damage in Mozambique equal to $550 million USD (LBPTC, 2010; LIMCOM, 2016). The area also undergoes significant periods of drought during ENSO events that can be detrimental to crop productivity. During the 2015/2016 drought, crop failure occurred in 20% of Mozambique's croplands, resulting in food insecurity for 1.5 million people.

Mozambique has the third lowest water demand of all countries in the LRB, with only Botswana using less (LBPTC, 2010). However, due to the catchment's location at the outlet of

the basin, water quality and quantity in the LLRB are degraded by upstream activity. Mining and irrigation by upstream users can result in contamination from metals and fertilizer. Upstream communities often abstract water from the river to use for irrigation, particularly during the dry season (FAO, 2004). Over-abstraction can lead to flow reductions in water shortages in downstream communities, as has been observed the Chokwe gauging station (LBPTC, 2010). Hydrologic infrastructure, such as dams and levees, can also limit the flow of the river and reduce sediment supply. The retention of sediment by dams and reductions in river flow can negatively impact the equilibrium of downstream delta-like environments in the lower Limpopo River basin. Without natural replenishment from sediment deposition, the river valley is susceptible to subsidence. Maintained flow rates are also essential for keeping saltwater in the Limpopo River estuary from intruding farther upstream (LIMCOM, 2013).

According to Petrie et al (2015) the LRB is already experiencing water closure, meaning that there is not enough water available to meet demand. In the LLRB, present water use is approximately 270 x 10^6 m^3/yr, and there is already not enough water to support the Chokwe Irrigation Scheme Irrigation developments, particularly for rice and sugar cane. Agricultural development could increase current water demand to about 1,200 x 10^6 m^3/yr in the future (LBPTC, 2010). Van der Zaag et al (2010) produced model simulations that demonstrated the Limpopo River can only support approximately 44,000 ha of newly irrigated land, which equates to only 60% of planned developments. Insufficient water supplies could increase reliance on groundwater resources in the LLRB and create tension among water users.

In recent years, stakeholders in the LLRB have expressed concerns about increasing salinity of water around Xai-Xai, particularly from June to September (Sharp & Kahler, 2019). Nhassengo Somura & Wolfe, 2021). Natural saltwater intrusion occurs in the Limpopo River

estuary for the 35 km upstream of river mouth, according to LIMCOM (2013). However, increasing saltwater intrusion farther upstream could lead to soil salinization and contamination of important surface and groundwater sources that are used for crop irrigation, drinking water and domestic use, and municipal/industrial supplies. River flow reductions, as well as increasing sea-level, can allow saltwater to penetrate farther upstream, as demonstrated in He et al (2018). Along with salinization of surface water, groundwater pumping can change the hydraulic head pressure and allow for lateral encroachment of saltwater into freshwater aquifers, a process which can contaminate groundwater wells (Loáiciga, 2011).

Political unrest and wartimes have made it difficult to maintain successful irrigation infrastructure and establish policies regarding crop production in the LLRB (FAO, 2004). Data regarding the status of surface and groundwater resources is limited through the entire basin, and historic records are typically incomplete or non-existent (LBPTC, 2010; LIMCOM, 2013). Improvements and standardization of data collection protocols must be implemented across the riparian states, and data sharing between countries will be essential to protect users from water scarcity and degradation, particularly those that live in downstream communities. Attempts have been made to protect the LLRB from degradation by upstream use under the TWM approach; however, to date no formal legislation has been passed to preserve minimum flows or water quality.

1.5 OBJECTIVES AND GUIDING CONCEPTS

Geophysical characteristics of the lower Limpopo River Basin and water use behavior increase the potential for land subsidence in the area. The underlying geology of the LLRB, which is primarily composed of unconsolidated sand, silt, and clay alluvium, is susceptible to natural compaction. Additionally, groundwater extraction is the leading driver of anthropogenic

land subsidence and is used in the LLRB for Xai Xai's municipal supply, domestic supply, and intense irrigation operations in the floodplain. Dams on the Olifants River at Massingir and Limpopo River at Macarretane could also contribute to the occurrence of land subsidence by reducing sediment deposition in the lower floodplain. Lastly, reports from stakeholders of elevated salinity levels in ground and surface water sources indicate that land subsidence could be increasing the rate of relative sea level rise, allowing for the landward intrusion of saltwater. Therefore, this study aims to determine if land subsidence is occurring the lower Limpopo River Basin and its potential contribution to reported increases in salinity.

To understand the role that land subsidence may be having on saltwater intrusion in the LLRB, three factors were evaluated: ΔGround Level, ΔRiver Height and ΔSea Level. To quantify these variables, we utilized spaceborne interferometric synthetic aperture radar (InSAR) from the Copernicus Sentinel-1 mission to detect potential land subsidence during the dry seasons (May to October) of 2017 to 2021. Changes to the height of the Limpopo River were assessed using in-situ hydrometric gauges at Chokwe and Xai-Xai. Eustatic sea-level rise data was collected from a tide gauge station located in Durban, South Africa. By comparing relative changes in the height of the land, river, and ocean, we can determine if the hydrostatic pressure relationship in Limpopo River estuary is allowing for farther landward movement of freshwater-saltwater interface. We hypothesize that land subsidence is occurring within the lower Limpopo River Basin at a rate that, when combined with sea level rise and river height changes, is contributing to increased saltwater intrusion upstream in the Limpopo River.

This study provides an innovate approach to assessing coastal resiliency in the lower Limpopo River basin. To date, there have been no subsidence studies conducted that have focused on the alluvial systems of the lower Limpopo River. Multiple studies have been

conducted investigating the impact of river flow and sea level on saltwater intrusion in estuarian environments; however, these studies rarely integrate land subsidence into their methods (He et al, 2018). Understanding the factors that are contributing to worsening saltwater intrusion is of vital importance in the LLRB, as the region relies heavily on access to clean, freshwater, and healthy floodplain soils to support their large agricultural operations. By evaluating the role of land subsidence and other hydrologic factors that contribute to saltwater intrusion, we can inform better water management practices and improve future data collection to protect the livelihoods of coastal communities in the LLRB. This study also demonstrates the benefit of using freely available, remotely sensed data for coastal risk assessments, particularly in countries where field data is limited.

CHAPTER 2: MATERIALS AND METHODS

2.1 LAND SUBSIDENCE DETECTION WITH INSAR

2.1.1 BASICS OF INSAR THEORY

Interferometric synthetic aperture radar, hereby known as InSAR, is a remote sensing technique that measures differences in phase, known as phase shifts, captured between two SAR images taken of the same area at different times (Osmanoğlu et al., 2016). The phase shift between the earlier image (primary) and later image (secondary) are displayed as repeating, colored fringes in data maps known as interferograms. Interferograms can be processed to show relative ground deformation, as is explained farther in this section. The wavelength of the satellite, equal to 360 or 2π radians, controls the amount of ground deformation represented by each colored fringe. For example, each colored fringe produced by Sentinel-1 interferograms represents half a wavelength worth of movement, or 2.8 cm. The color progression of the interferogram fringes is indicative of movement direction, either toward the satellite (uplift) or away from the satellite (subsidence).

Phase shifts that are recorded in interferogram fringes contain the following components:

$$\Delta\varphi InSAR = \Delta\varphi disp + \Delta\varphi flat + \Delta\varphi elev + \Delta\varphi atm + \Delta\varphi noise \quad (1)$$

where,

ΔφInSAR = Total interferometric phase signal

Δφdisp = Phase contribution from surface displacement

$\Delta\varphi$flat = Phase contribution due to the curvature of the Earth's surface

Δφelev = Phase contribution from topography

Δφatm = Phase contribution from changes in atmospheric conditions

Δφnoise = Phase noise introduced by changes to surface scattering properties

The basic theory behind InSAR for deformation monitoring is to remove all phase contributions, aside from displacement. The contribution from flat Earth phase ($\Delta\varphi$flat) can be removed using precise orbital information (perpendicular baseline) recorded by the satellite. In traditional InSAR methodology, the phase contribution from topography ($\Delta\varphi$elev) can be used to create elevation maps. This technique was first used to create topography maps of Venus (Rogers & Ingalls, 1969). However, when using InSAR for deformation monitoring, removing the phase contribution from topography is a necessity and is referred to as Differential Interferometry (DInSAR) (2). Removal of the topographic phase can be done with a digital elevation model (DEM) such as the models produced by the Shuttle Radar Topography Mission (SRTM).

$$\Delta\varphi DInSAR = \Delta\varphi disp + \Delta\varphi atm + \Delta\varphi noise \quad (2)$$

Δφatm is caused by the propagation of electromagnetic waves through the atmosphere. The velocity of electromagnetic waves traveling through air is slower than if they were travelling through a vacuum. The change in velocity of the signal as it moves through the atmosphere creates phase shifts that are not attributed to land deformation. Phase contribution from the atmosphere depends on air temperature, air pressure and humidity and can be removed using a tropospheric delay model.

The last contribution that will need to be removed is contribution from noise, which appears into interferograms as speckles. The most common cause of noise is temporal changes to scatterers in the period between the SAR acquisitions. Noise is prevalent over vegetated areas, one of the main limitations to InSAR, as well as bodies of water because these environments change their reflection surfaces within seconds. Noisy SAR signals can sometimes be removed using spatial averaging or filtering techniques, although many of these techniques are still being

developed. With all other phase contributions now removed, the interferograms should only contain the phase shifts directly related to ground deformation.

Because the phase measurements of deformation are wrapped between cycles of -π to π, they only provide relative, ambiguous measurements and contribute little to deformation mapping. Essentially, wrapped interferograms demonstrate that a phase shift has occurred but not how many integer wavelengths it took to obtain that phase shift signal. Therefore, wrapped interferograms must undergo "unwrapping" which is the process by which correct integer multiples of 2π are added to interferometric fringes (ESA, 2007). Unwrapped interferograms provide actual measurements of the actual altitude variation. Unwrapping is the most complex aspect of InSAR data processing, and over the years several algorithms have been developed to improve this step.

After the interferograms are unwrapped, phase values in radians can be converted into displacement (d) measurements in meters along the line-of-site (LOS) direction using the equation:

$$d = -\lambda/4\pi(\Delta\emptyset_d) \quad (3)$$

where λ is the SAR wavelength and $\Delta\emptyset_d$ is the unwrapped phase shift between the primary and secondary image. Velocity in the LOS direction means that ground movement is detected towards or away from the satellite at the angle the image was captured at. LOS captures deformation in both the horizontal and vertical components of movement but cannot distinguish between the two unless farther processing is completed.

2.1.2 INSAR TECHNIQUES

InSAR has classically been used for hazard monitoring of rapid events such as fault movement during earthquakes and landslides. For these studies, a small number of SAR images

are analyzed to compare conditions immediately before and after the event. For quantification of slow, long-term movement, such as subsidence related to groundwater extraction, there are two dominant time-series (TS-InSAR) techniques that are utilized. These are the PS (Persistent Scatter) technique or short-baseline subset (SBAS) technique.

PS-InSAR involves the identification of SAR pixels that have a strong and constant reflection over a long period (Crosetto et al, 2015). In this technique, all secondary images are compared to the same primary image and only the PS pixels are used in the deformation calculations. Persistent scatterers are typically hard, stable objects such as buildings, bridges, and rock faces. This technique provides excellent monitoring capabilities for urban areas, bare rock and primarily used for monitoring bare rock and urban areas The SBAS technique creates a network of unwrapped interferograms with short temporal baselines to monitor displacement in small increments for a long time-period (Berardino et al, 2002). This technique reduces the effects of temporal decorrelation is superior for measuring slow ground displacement and vegetated areas. Due to the heavy amounts of crop growth in the Limpopo River valley, the SBAS technique was selected for this analysis.

2.1.3 SAR DATA ACQUISITION AND INSAR PRE-PROCESSING

The Copernicus Sentinel-1 mission, led by the European Space Agency (ESA), consists of two near-polar (98.18°) orbiting satellites: Sentinel-1A (S1A) and Sentinel-1B (S1B). Launched in April 2014 and April 2016, respectively, S1A and S1B are equipped with a C-band, synthetic aperture radar (SAR) which allows for collection of data day or night, regardless of cloud cover. S1A and S1B each have a 12-day repeat cycle, however, with 180° orbital separation a shortened 6-day repeat cycle can be achieved if images from both satellites are used. The primary imaging mode over land is interferometric wide-swath (IW) which produces a 250

km swath. For InSAR analysis, single-look complex (SLC) acquisitions, which contain both phase and amplitude information, are required.

The Alaska Satellite Facility (ASF) short-baseline subset (SBAS) tool was used to generate a network of interferometric pairs, composed of primary and secondary SAR images of the LLRB with short temporal baselines between them. Due to the computationally intense nature of InSAR processing, ASF's Hybrid Pluggable Processing Pipeline (HyP3) was used to generate and unwrap the interferograms for each pair. HyP3 uses the GAMMA software for InSAR processing. GAMMA processing consists of orbital corrections and flat Earth phase removal, topographic phase removal with a DEM, coregistration to align the image pixels and spectral filtering to limit noise. Then, it produces the wrapped and unwrapped interferograms, as well as additional product files, with an 80-meter spatial resolution that can be loaded into MintPy for SBAS time-series processing.

2.1.4 SBAS TIME-SERIES ANALYSIS WITH MINTPY

The Miami INsar Time-series software in PYthon (MintPy) is an open-source, InSAR time-series analysis package, designed for the small-baseline InSAR technique (Yunjun et al., 2016). MintPy implements a weighted least squares inversion to convert a stack of coregistered, unwrapped interferograms into 3-dimensional ground surface displacement measurements in the line-of-sight (LOS) direction. The program is compatible with a variety of InSAR pre-processing softwares, including ISCE, ARIA, FRInGE, SNAP, ROI_PAC and HyP3.

MintPy uses a series of parameters to remove noisy or poorly correlated interferograms. For this analysis, interferograms with an average spatial coherence < 0.5 were removed from the network. This parameter was selected through trial and error, as coherence values greater than 0.5 removed too many interferograms from the network. Individual pixels

with an average temporal coherence of < 0.7 were also filtered out before the inversion took place. This parameter was selected because it is the standard, recommended value for temporal coherence masking according to Yunjun et al (2016). To correct interferograms for the spatial and temporal variations in tropospheric conditions, the ERA-5 tropospheric delay model from the European Center for Medium-Range Weather Forecast (ECMWF) was used (Jolivet et al., 2011). Data that was included in the model includes air temperature and pressure, and specific humidity for each day an image was taken.

Because MintPy analyzes relative motion, a reference pixel must also be set. The reference pixel is an area which is assumed to be stable and unmoving over time. For this analysis, a reference pixel at -25.038°S, 33.741°E, located in the western part of the Xai-Xai district, was selected. This pixel was initially selected due to the presence of a GNSS beacon. GNSS data has proven useful in other subsidence studies for validating InSAR results (Ge et al., 2001). However, data from this station was ultimately not able to be obtained. Despite this limitation, this reference pixel exhibited high coherence and was located outside of the Limpopo River valley.

2.2 RIVER HEIGHT

River height data was collected from Regional Administration of Aguas do Sul (ARA-SUL) from station E-35 at Chokwe, Mozambique and station E-38 at Xai-Xai, Mozambique (Tivane E., & Silva A., email, May 11, 2022) These gauges record daily mean measurements of water height in meters. Daily mean height values were converted to yearly averages based on the hydrologic year in southern Africa (August 1 to July 31). This process was completed for the periods of 1996 to 2019 and 2000 to 2019 for Xai-Xai and Chokwe, respectively.

2.3 SEA LEVEL

Sea-level rise was evaluated using daily mean water height recorded by a tide gauge in Durban, South Africa, located at -29.867°S, 31.050°E. Data from this gauge was downloaded from the University of Hawaii Sea Level Center (UHSLC) and converted into annual average sea-level measurements in cm based on hydrologic years (August 1 to July 31) from 1971 to 2017.

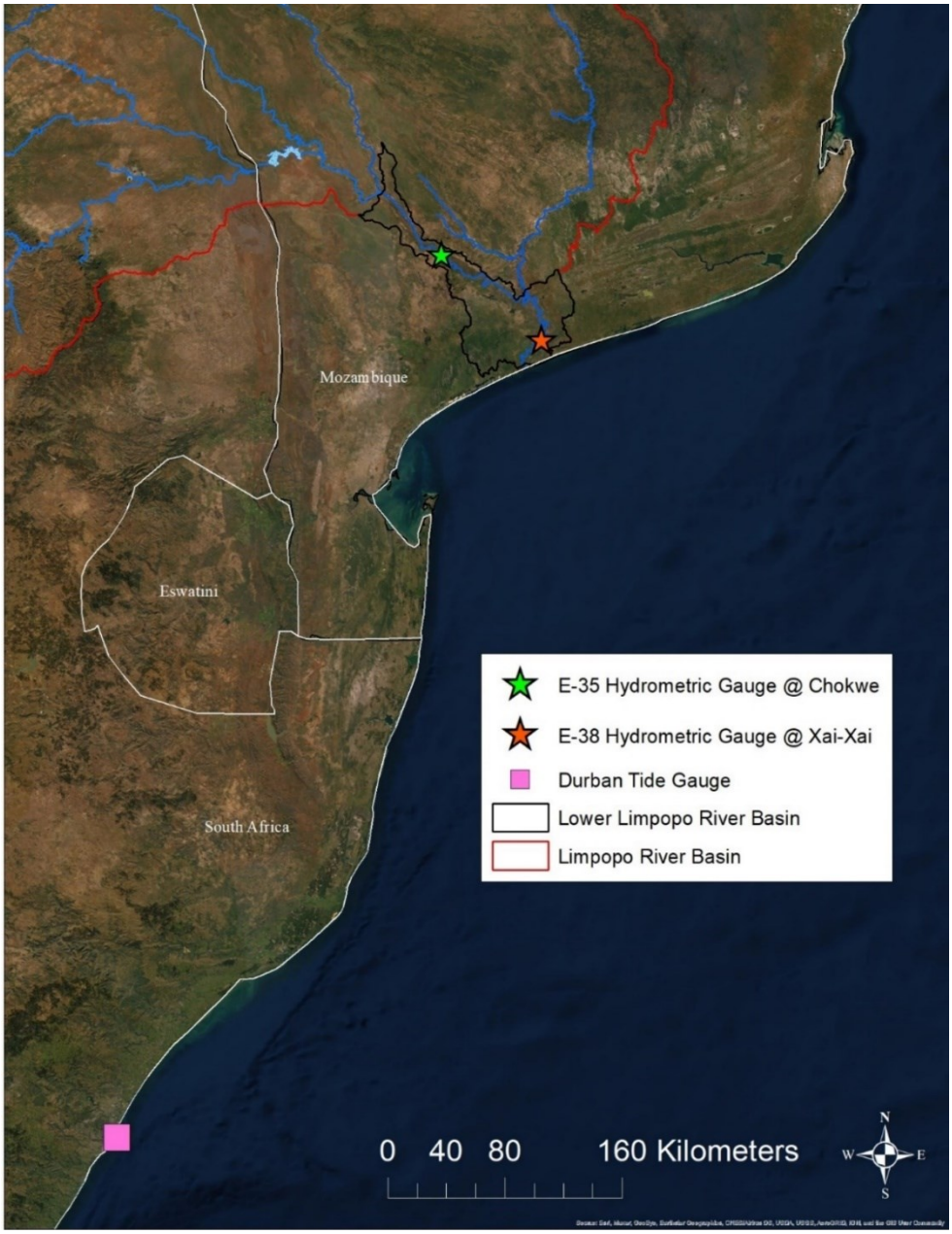

Figure 5: Location of Chokwe (E-35) and Xai-Xai (E-38) hydrometric gauges along the Limpopo River and Durban, South Africa tide gauge.

CHAPTER 3: RESULTS AND DISCUSSION

3.1 LAND SUBSIDENCE

3.1.1 COHERENCE AND NETWORK MODIFICATIONS

Preliminary attempts to generate a multi-year SBAS network failed due to low coherence of interferometric pairs that were generated from SAR images taken during the wet season from November to April. This trend was observed across all six dry seasons included in the network (Figure 6). Interferograms with low coherence, which indicate the presence of noisy and potentially inaccurate data, are removed by MintPy to assure accurate deformation velocity results. However, in this case, removal of low coherence interferograms resulted in an unconnected network, which is required for an SBAS analysis.

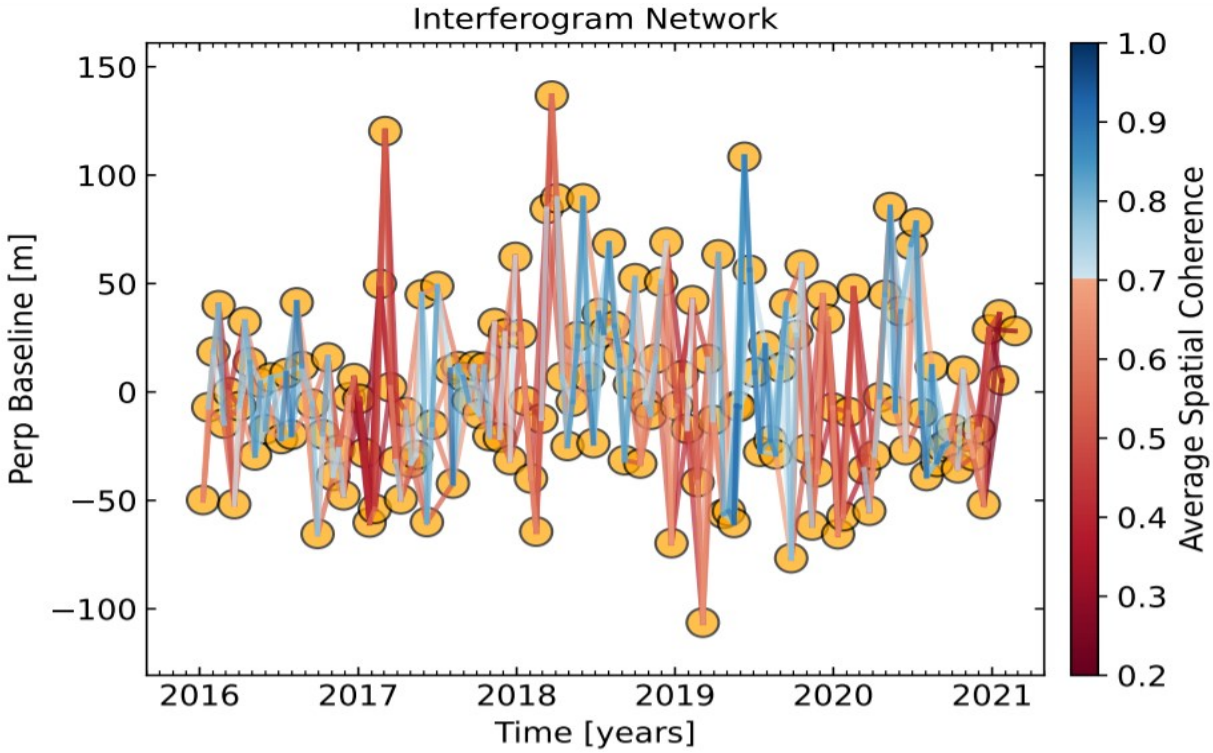

Figure 6: Preliminary results of multi-year SBAS network created from 2016 to 2021. Low coherence occurs in seasonal patterns, with a loss of coherence observed during the wet season (November to April).

Secondary trials, in which the wet seasons were bridged over by creating interferometric pairs with longer temporal baselines were also attempted. However, the interferograms with long temporal baselines also experienced low coherence, likely due to changing surface properties such as vegetation growth, that would have occurred during this time. Therefore, we elected to create 5 individual, SBAS networks, one for each dry season (May to October) from 2017 to 2021. It should be noted that, due to this approach, all velocity results are based on the assumption that the motion detected during the dry season months is consistent with deformation trends throughout the entirety of the year. It is possible that recharge during the wet season may allow for some degree of aquifer rebound, however, these trends are not able to be quantified in this analysis.

Spatial coherence remained generally consistent across the five dry seasons that were analyzed. Figures 7-11 show the average spatial coherence of the study area for each dry season, with pixels that are lighter in color corresponding to higher coherence (closer to 1.0) and dark pixels corresponding to lower coherence, or noise. High spatial coherence was observed in the built-up areas of Xai-Xai and Chicumbane, as well as portions of the Limpopo River valley. Low coherence is prevalent in saturated areas of the floodplain, which change from year to year, along with bodies water like the Limpopo River and smaller lakes throughout the study area. Dry season 2019 exhibited the highest average spatial coherence across the study with an average of 0.637 (Figure 10) and dry season 2017 exhibited the lowest at 0.543 (Figure 7).

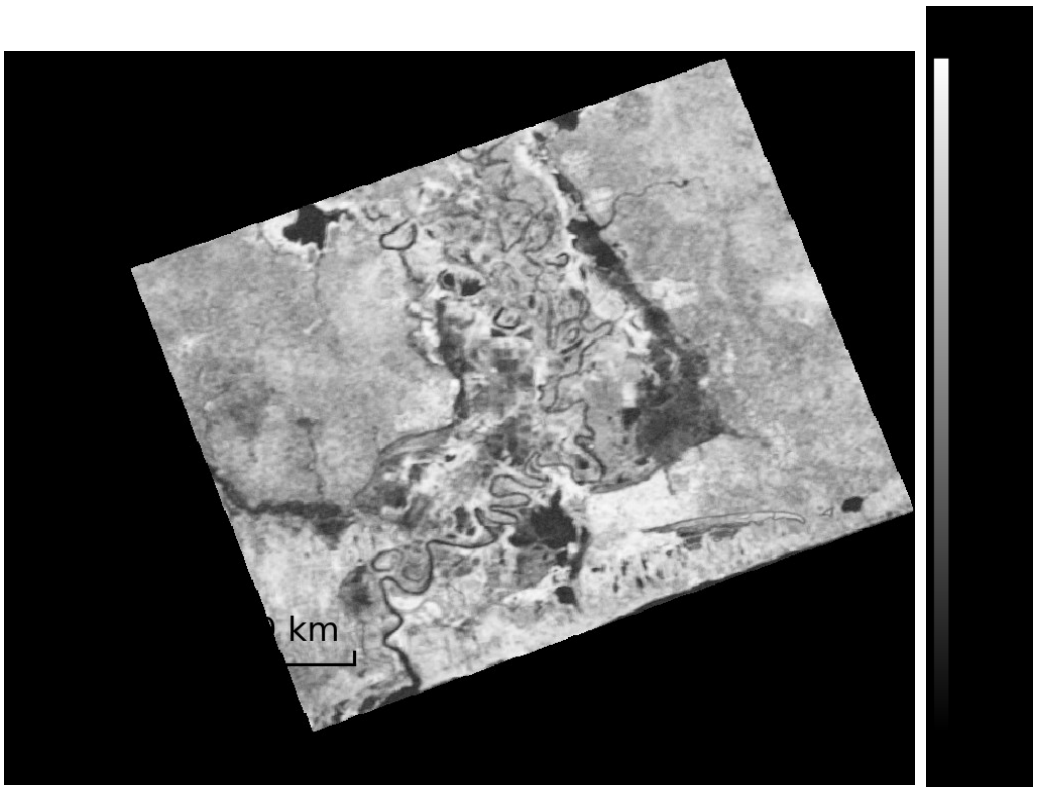

Figure 7: Average spatial coherence of 2017 dry season (mean = 0.543).

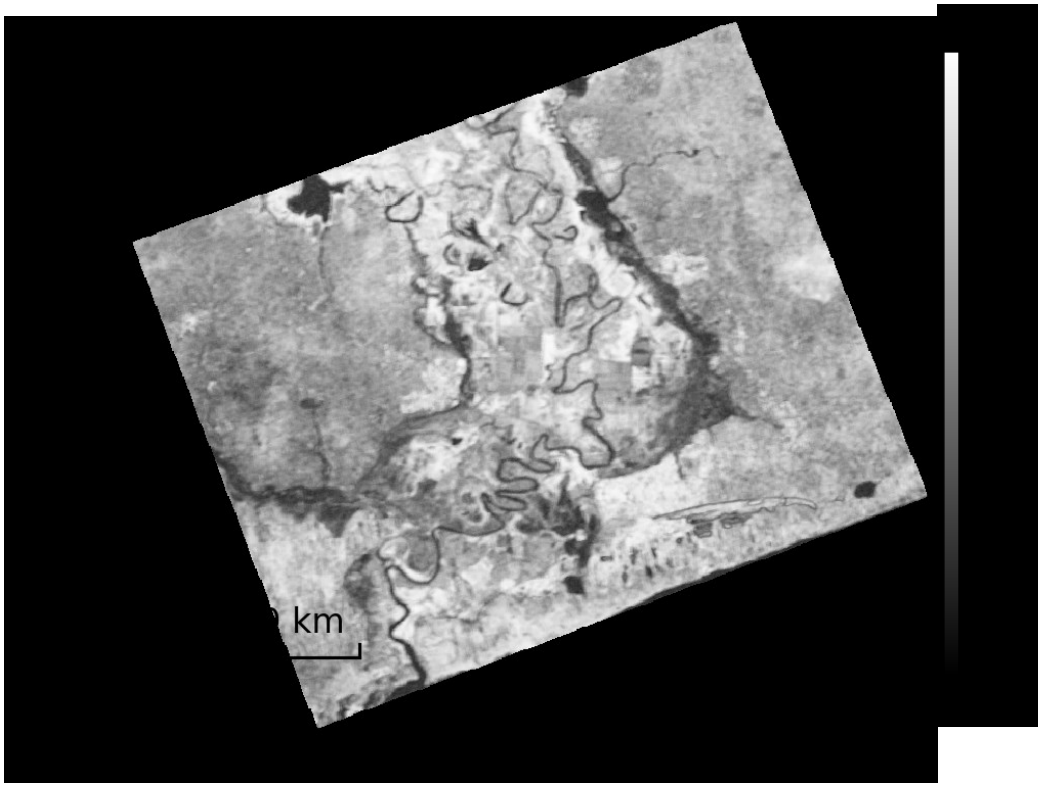

Figure 8: Average spatial coherence of 2018 dry season (mean = 0.589).

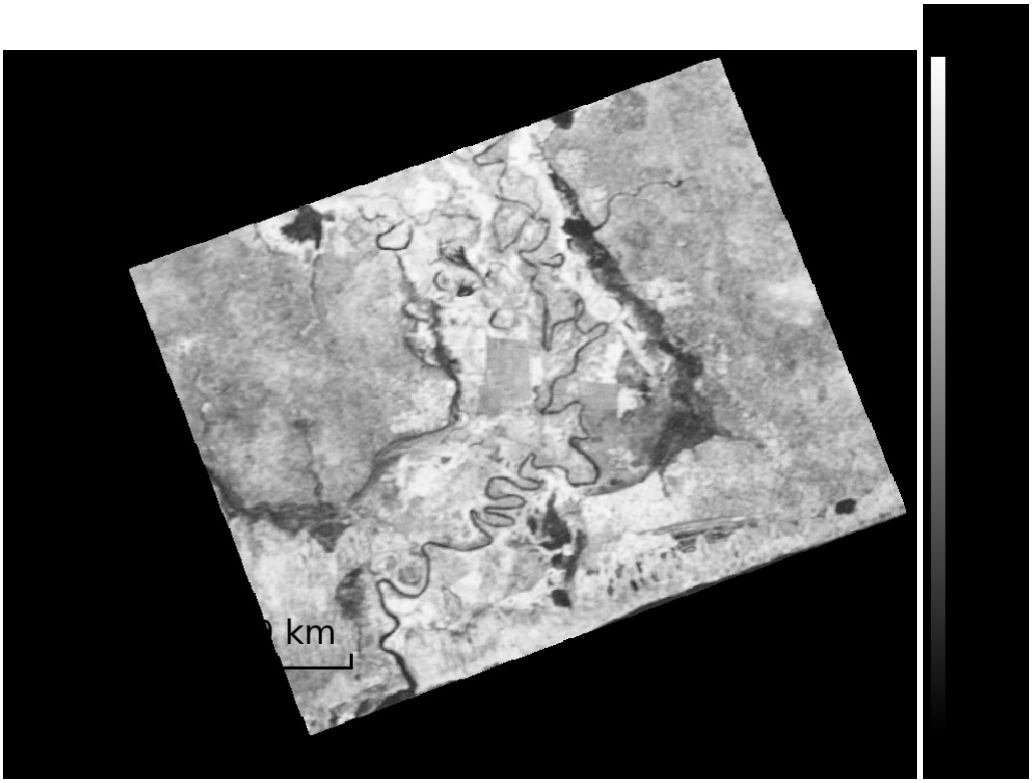

Figure 9: Average spatial coherence of 2019 dry season (mean = 0.637).

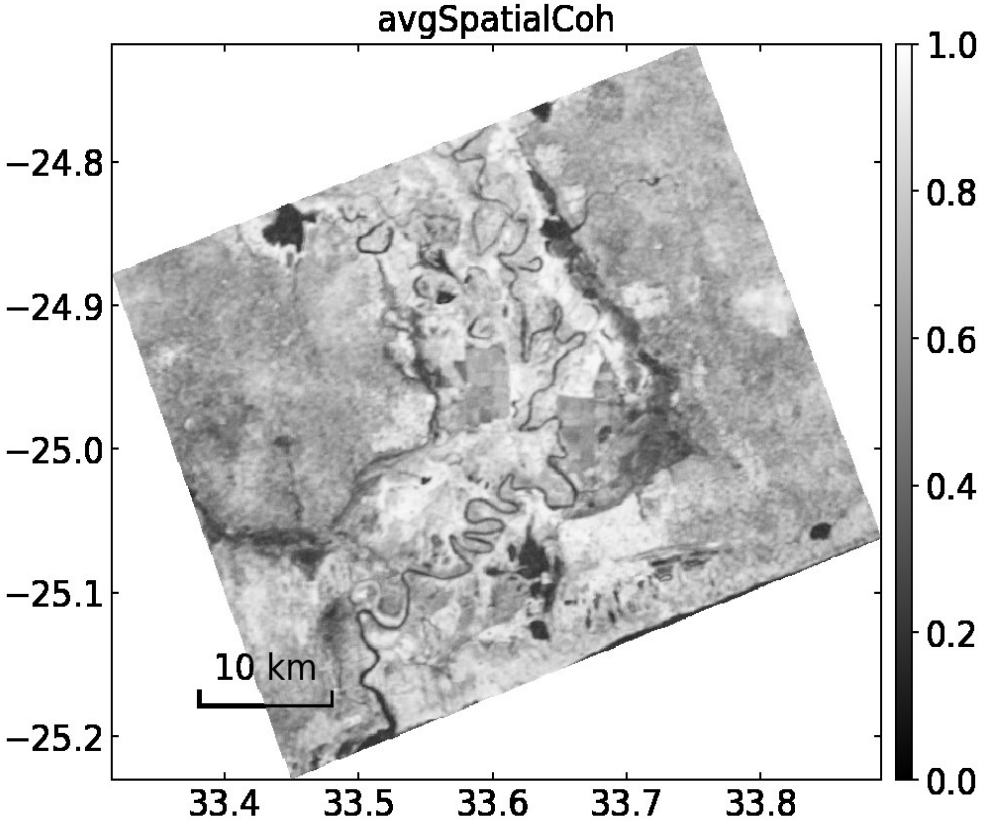

Figure 10: Average spatial coherence of 2020 dry season (mean = 0.589).

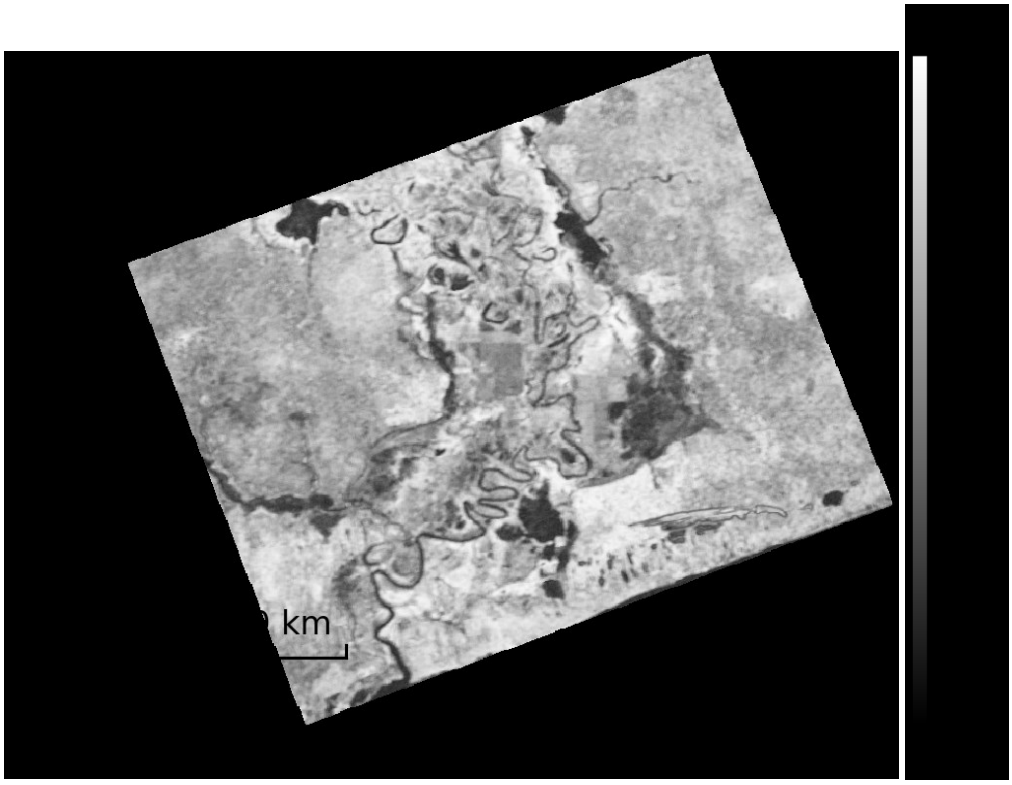

Figure 11: Average spatial coherence of 2021 dry season (mean = 0.557).

Figures 12-16 are the temporal coherence masks used to remove pixels from the interferograms that have temporal coherence values < 0.7. Unlike the spatial coherence figures, white pixels in figures 12-16 indicate that the coherence criteria were not met, and that pixel was removed. Variability can be seen when comparing the temporal coherence masks from across the five dry seasons, with the 2018 dry season (Figure 13) exhibiting a high number of removed pixels and 2017 (Figure 12) and 2021 (Figure 16) dry seasons exhibiting less pixel removal.

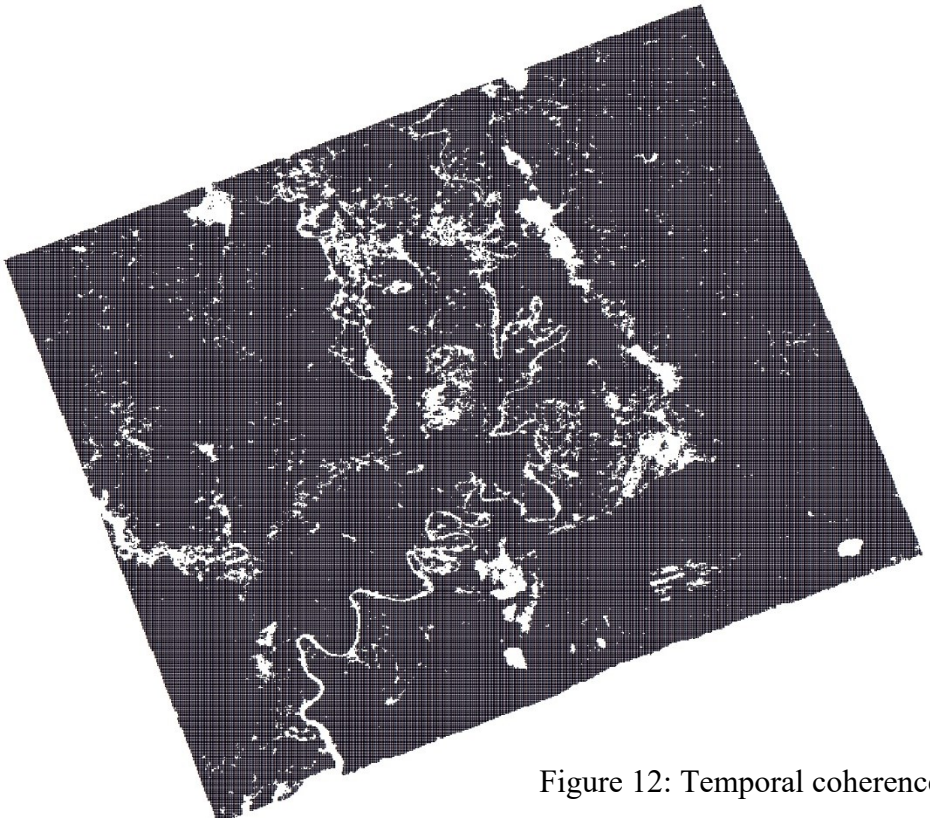

Figure 12: Temporal coherence mask for 2017 dry season.

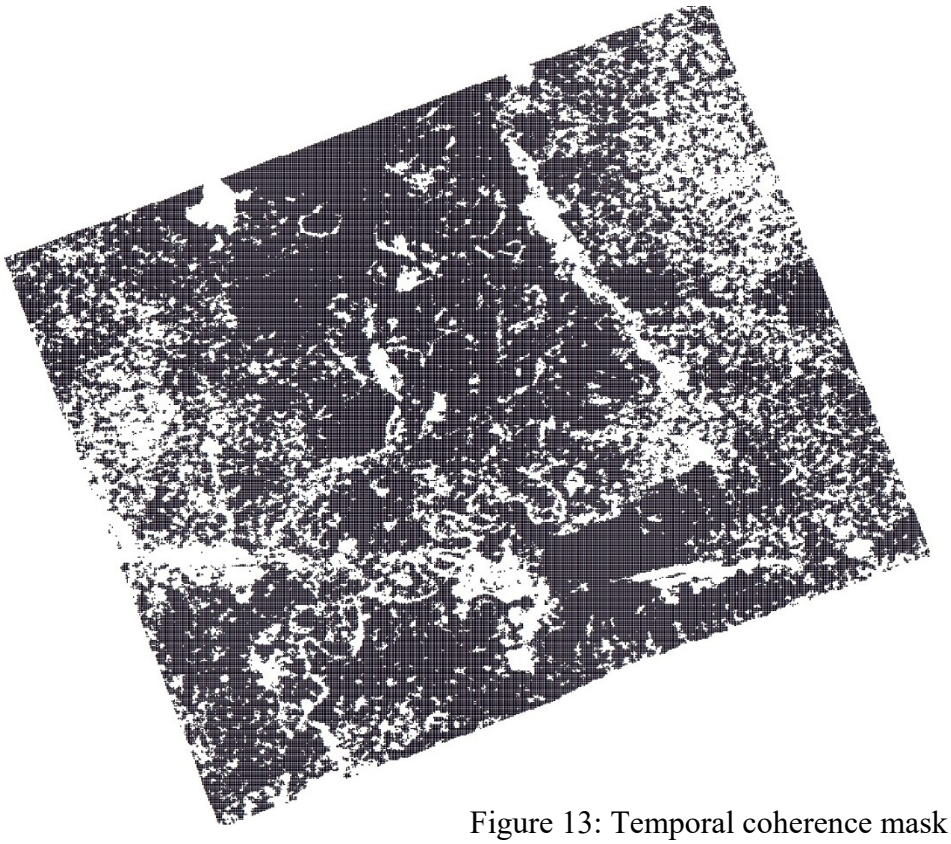

Figure 13: Temporal coherence mask for 2018 dry season.

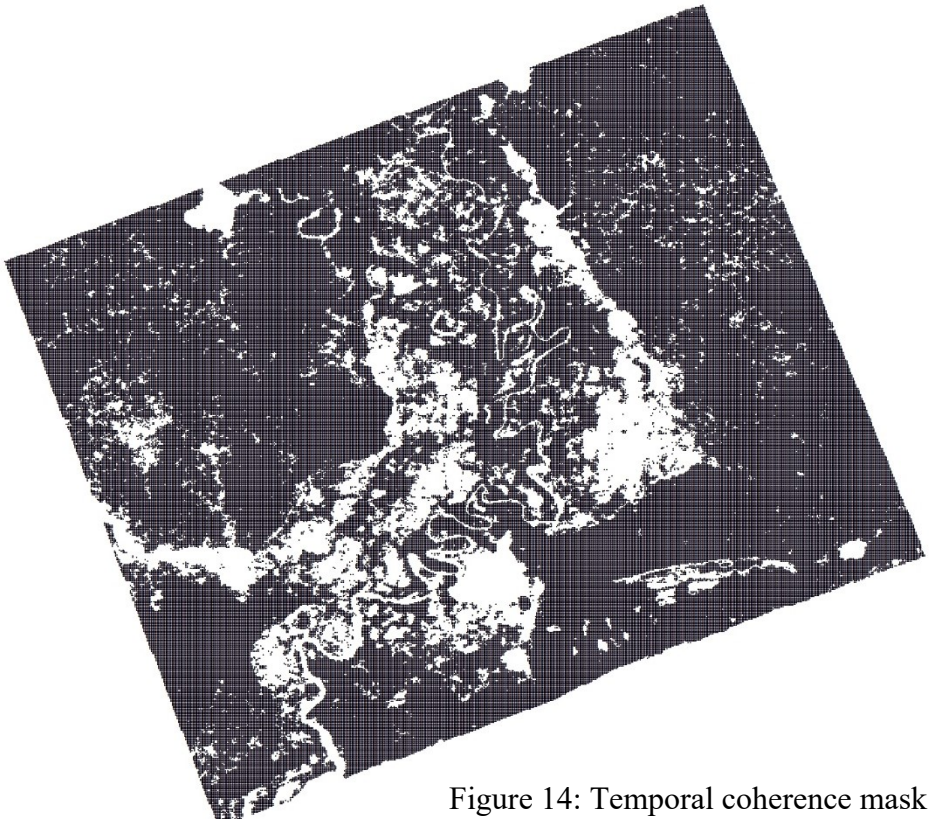

Figure 14: Temporal coherence mask for 2019 dry season.

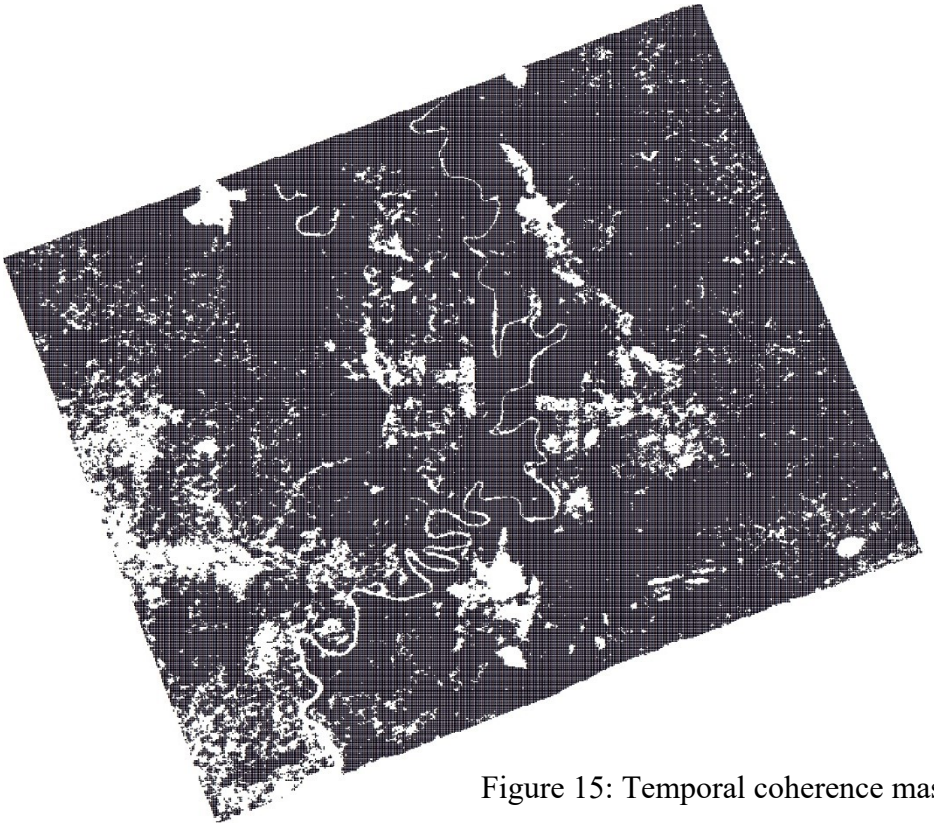

Figure 15: Temporal coherence mask for 2020 dry season.

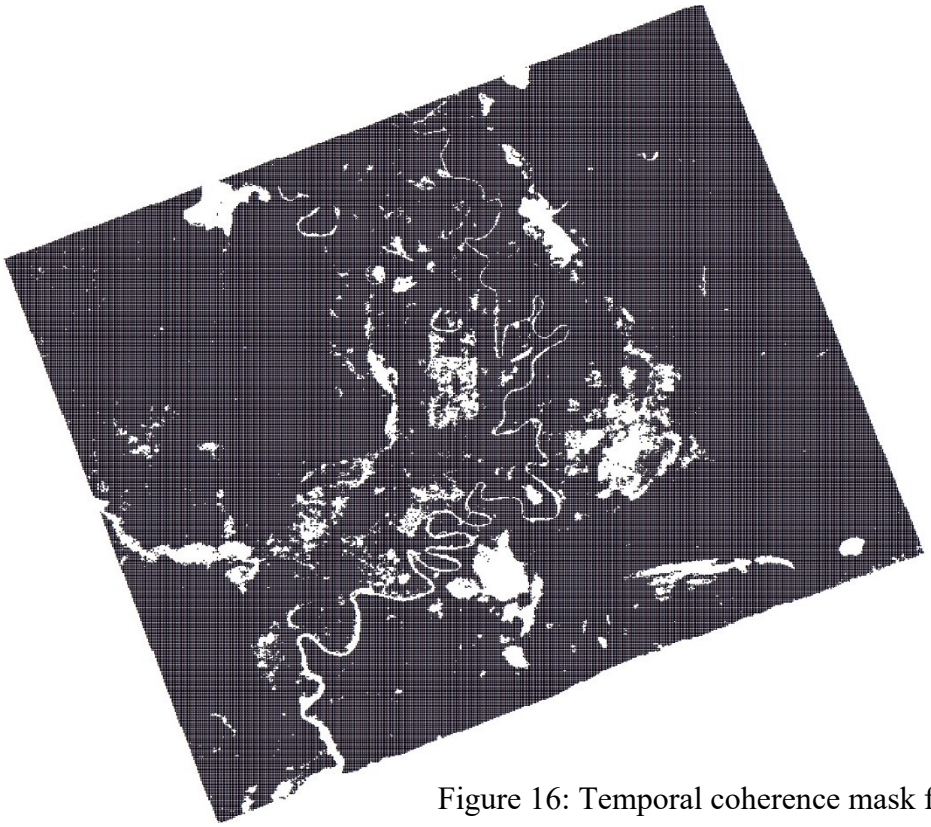

Figure 16: Temporal coherence mask for 2021 dry season.

The SBAS networks of interferograms that were used for the velocity calculations are shown in Figures 17-21. Yellow data points represent SAR acquisitions that were included in the velocity calculations, and grey data points represent SAR acquisitions that were removed because they were outside of the target date range. Red, dotted lines indicate interferograms that were removed from the network because they had an average spatial coherence less than 0.5.

A summary of the SBAS network modifications can be seen in Table 1. A total of 88 SAR images were collected across all five dry seasons and combined to create a network of 285 interferometric pairs. Then, 108 of those pairs were removed due to not meeting the coherence criteria in MintPy, leaving us with a total of 177 interferograms that were used to calculate the deformation velocity.

Table 1: Summary of image collection and network modification for the five SBAS networks.

Dry Season	Number of SAR Images Available	Number of InSAR Pairs Created with SBAS tool	Number of Pairs Removed with MintPy Parameters	Number of Pairs Used for Velocity Calculations
2017	19	55	27	28
2018	15	49	16	33
2019	20	61	15	46
2020	19	60	23	37
2021	15	60	27	33
TOTAL	**88**	**285**	**108**	**177**

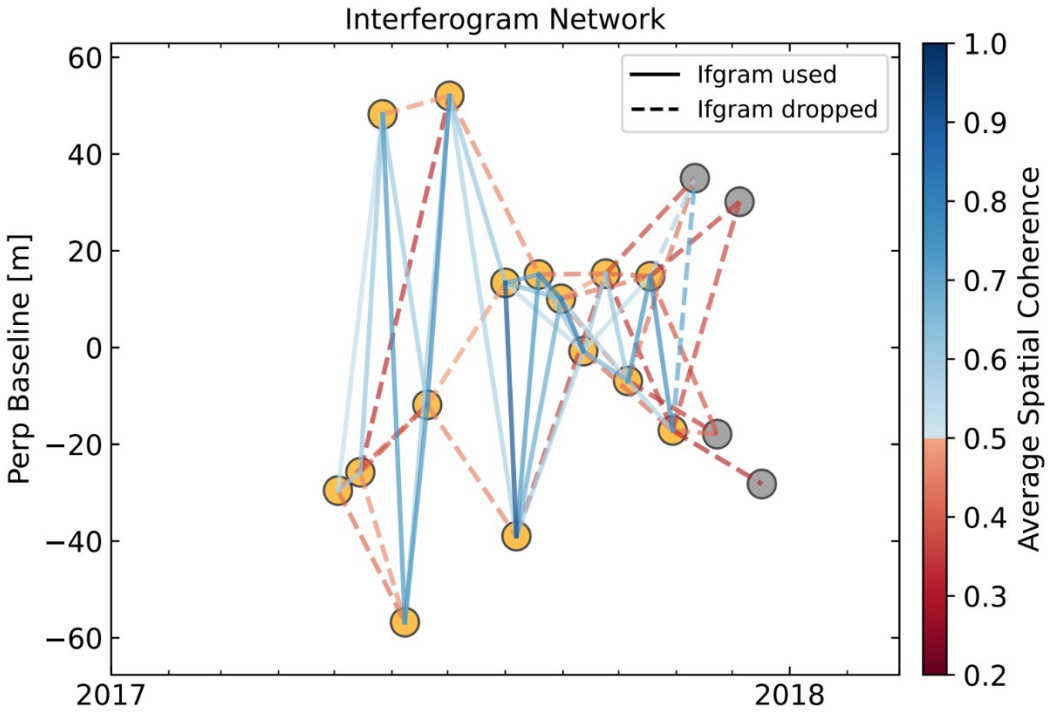

Figure 17: Network modifications for 2017 dry season analysis. Yellow circles represent acquisitions that were kept, and grey dots represent acquisitions that were dropped.

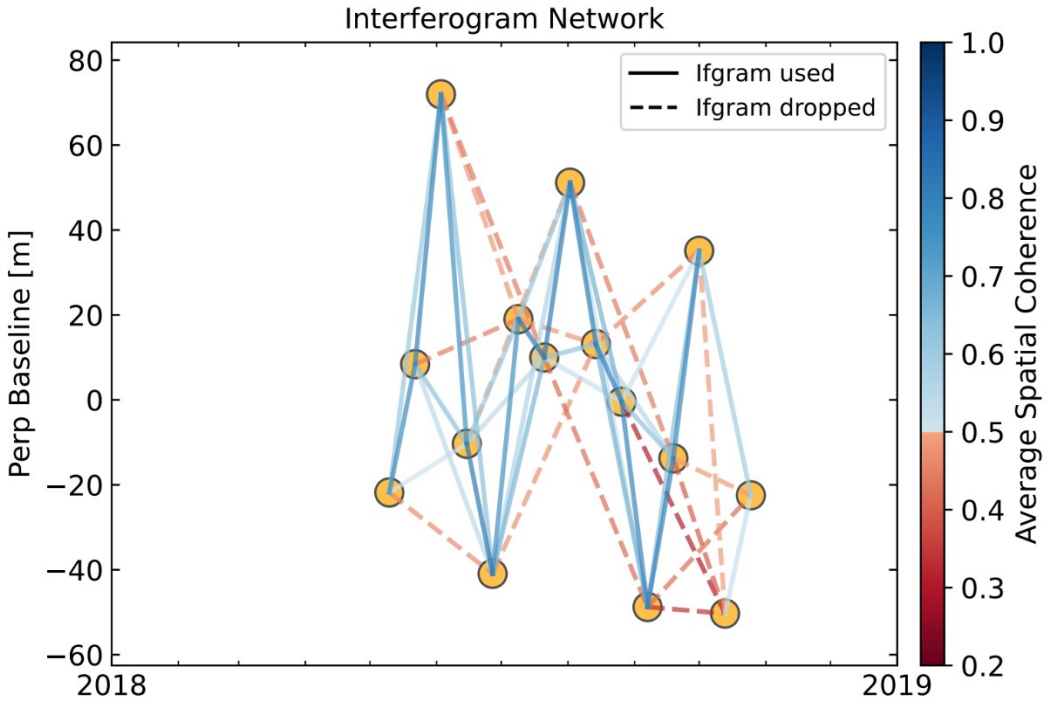

Figure 18: Network modifications for 2018 dry season analysis. Yellow circles represent acquisitions that were kept, and grey dots represent acquisitions that were dropped.

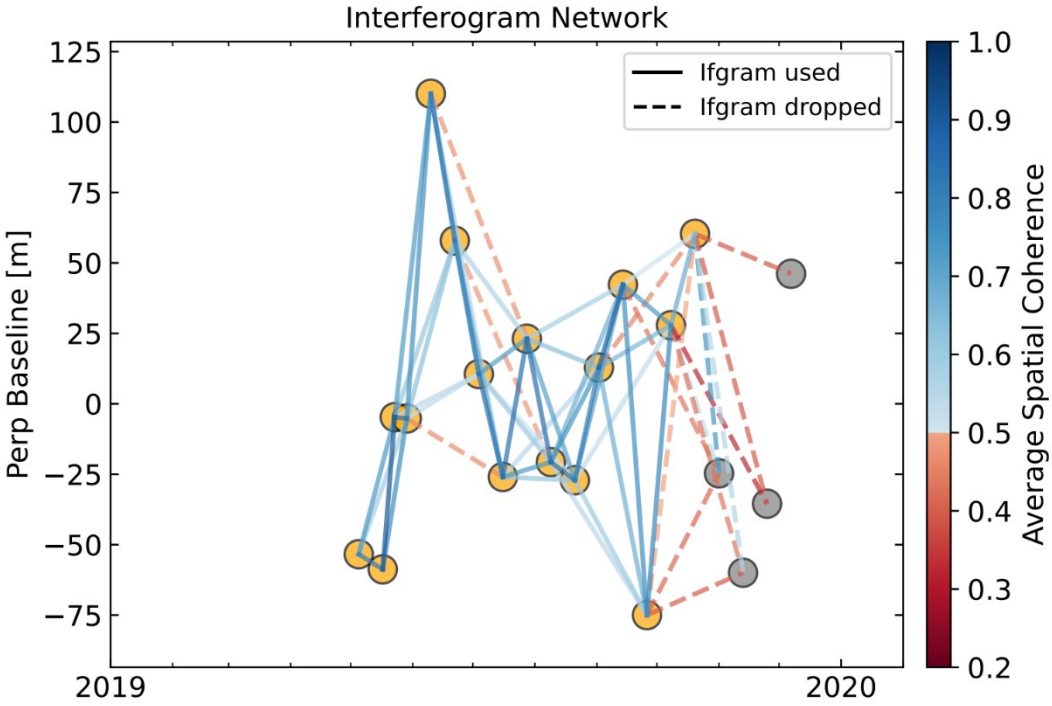

Figure 19: Network modifications for 2019 dry season analysis. Yellow circles represent acquisitions that were kept, and grey dots represent acquisitions that were dropped.

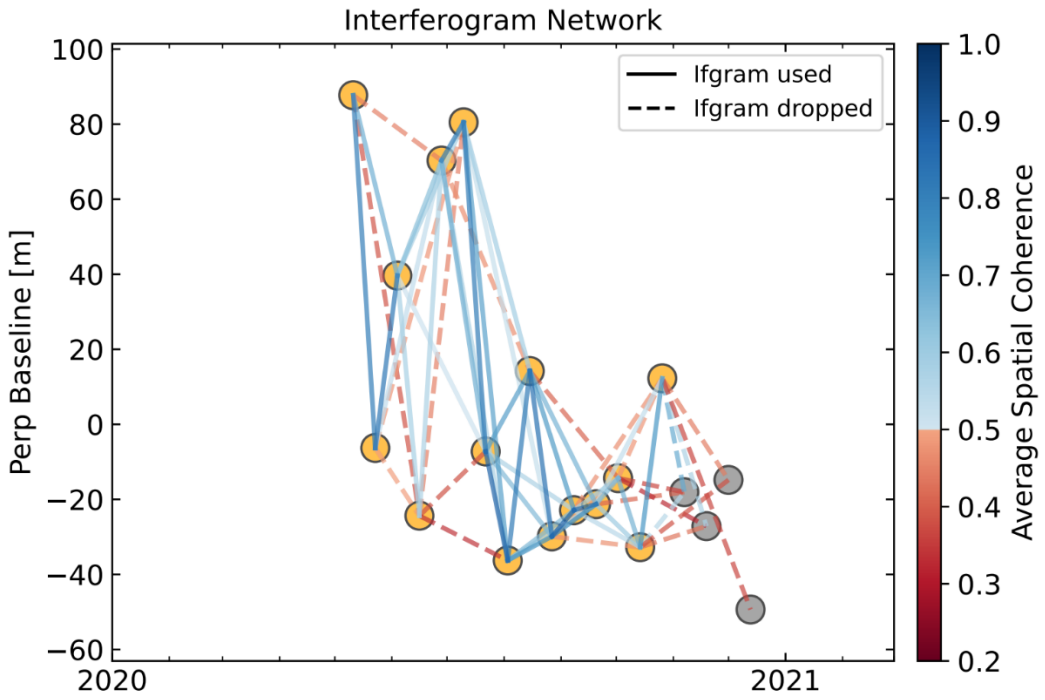

Figure 20: Network modifications for 2020 dry season analysis. Yellow circles represent acquisitions that were kept, and grey dots represent acquisitions that were dropped.

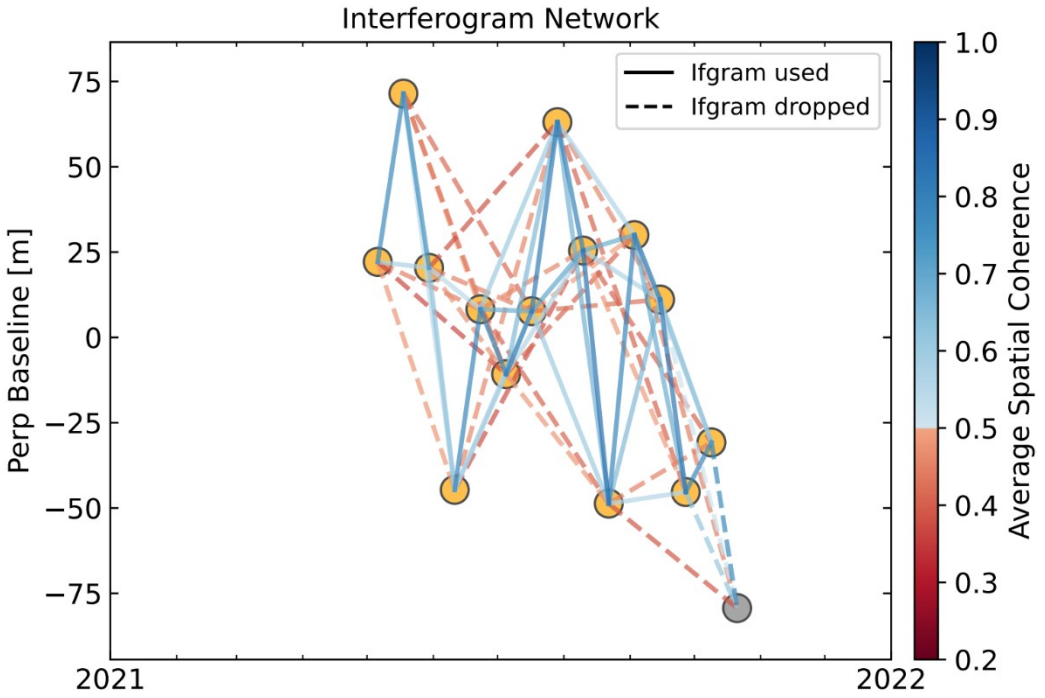

Figure 21: Network modifications for 2021 dry season analysis. Yellow circles represent acquisitions that were kept, and grey dots represent acquisitions that were dropped.

3.1.2. DEFORMATION VELOCITY

Results of the SBAS InSAR analysis indicate that subsidence has occurred in the LLRB for each of the five dry seasons that were studied. Subsidence is concentrated within the Limpopo River valley, shown in Figures 22-26, by the black dashed outline. Subsidence is prevalent in the area just north of the Xai-Xai for all dry seasons except for 2020 (Figure 25). Figures 22-26 have been modified by removing uplifting pixels. Interactive time-series KMZ files of the entire study area with the uplifted pixels were produced (SI 1).

Subsidence rates for all pixels within the Limpopo River Valley were averaged to determine in the average rate of river valley subsidence for each dry season. Again, it should be noted that these rates use the unit cm/yr. However, the actual displacement that occurred during the study time-period (May to October) will be less than that. Because our analysis only studied the dry season, any expansion of the surface that occurred from wet season recharge is not being captured.

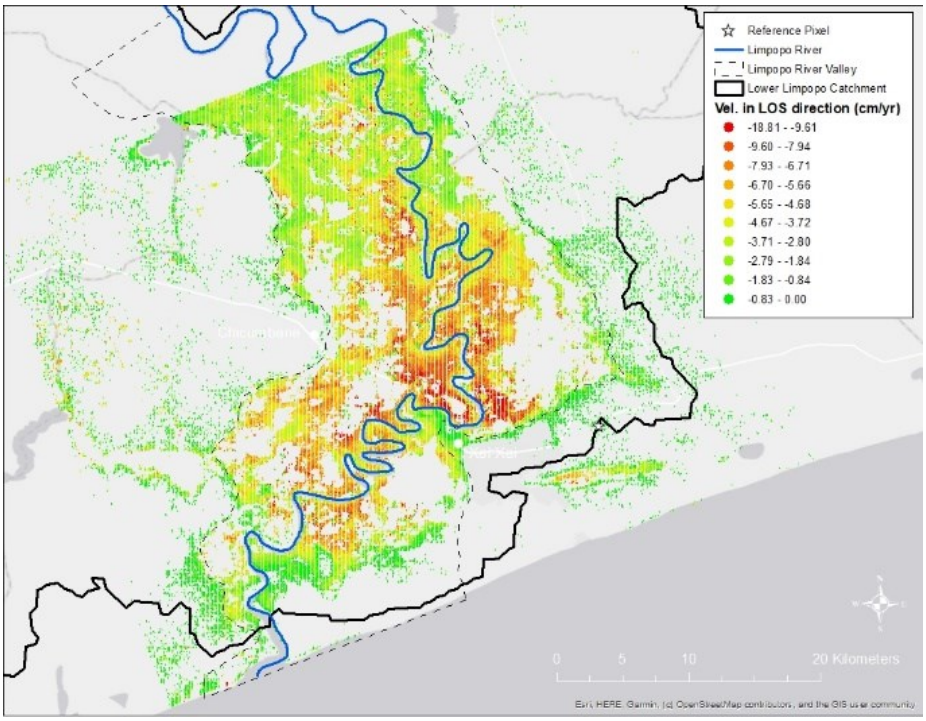

Figure 22: Subsidence results of the 2017 dry season. Uplifted pixels are not shown.

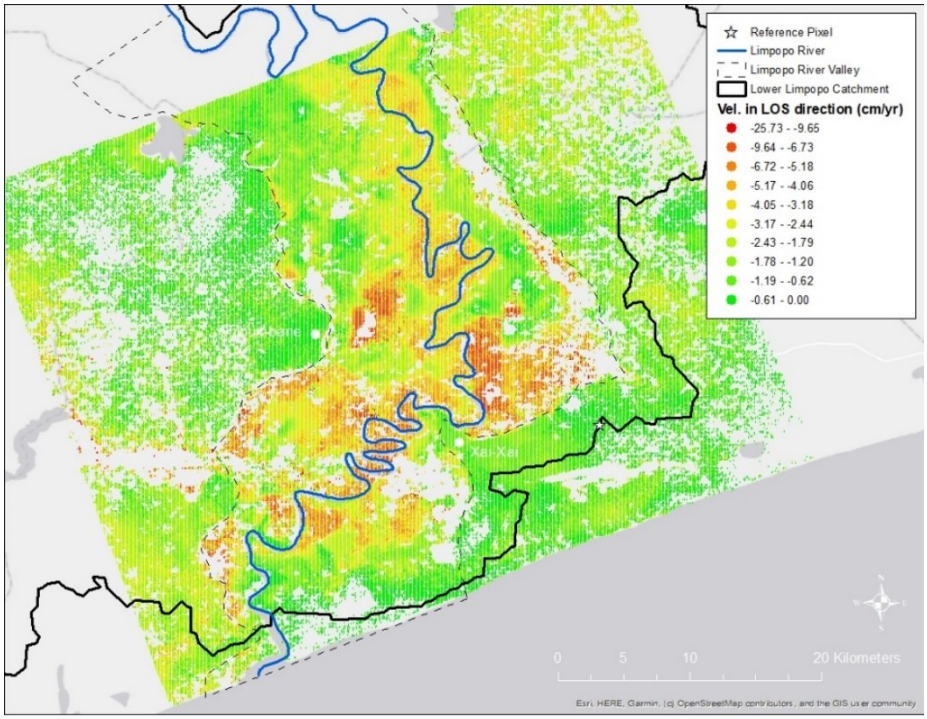

Figure 23: Subsidence results of the 2018 dry season. Uplifted pixels are not shown.

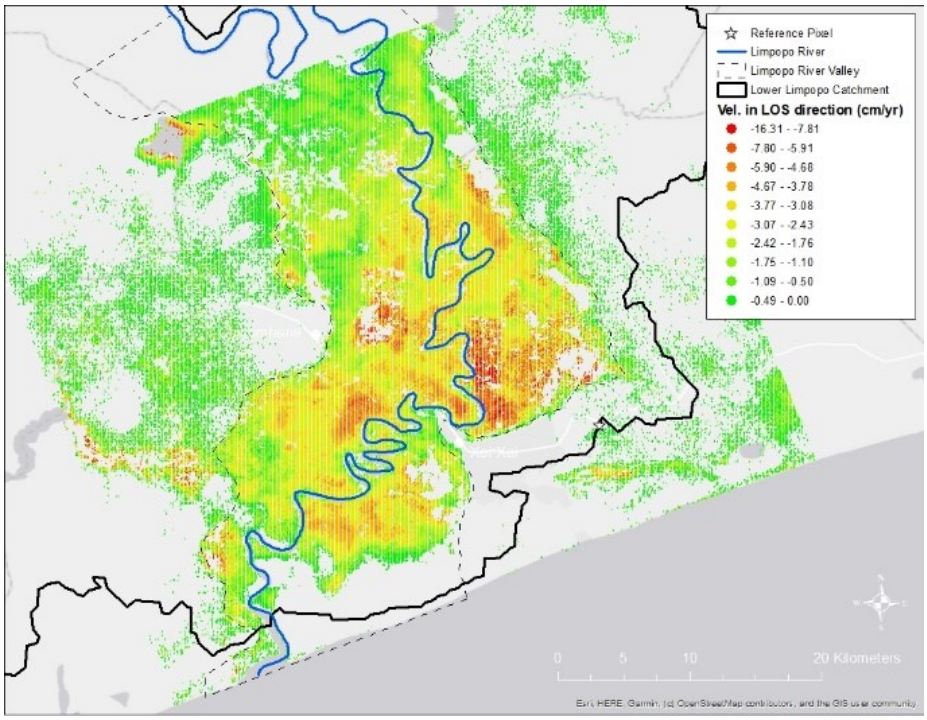

Figure 24: Subsidence results of the 2019 dry season. Uplifted pixels are not shown.

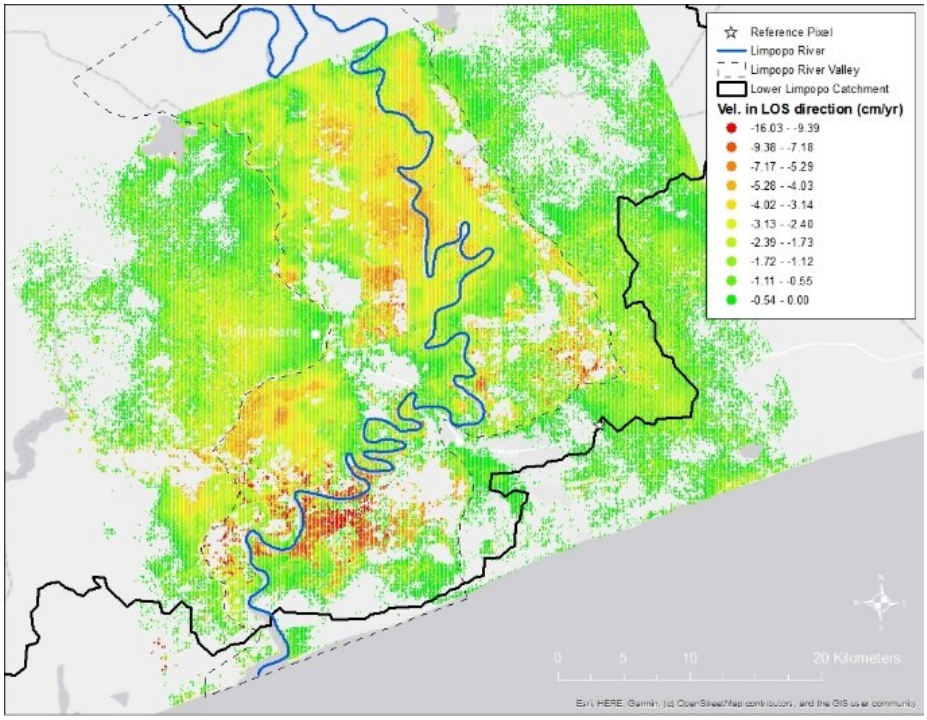

Figure 25: Subsidence results of the 2020 dry season. Uplifted pixels are not shown.

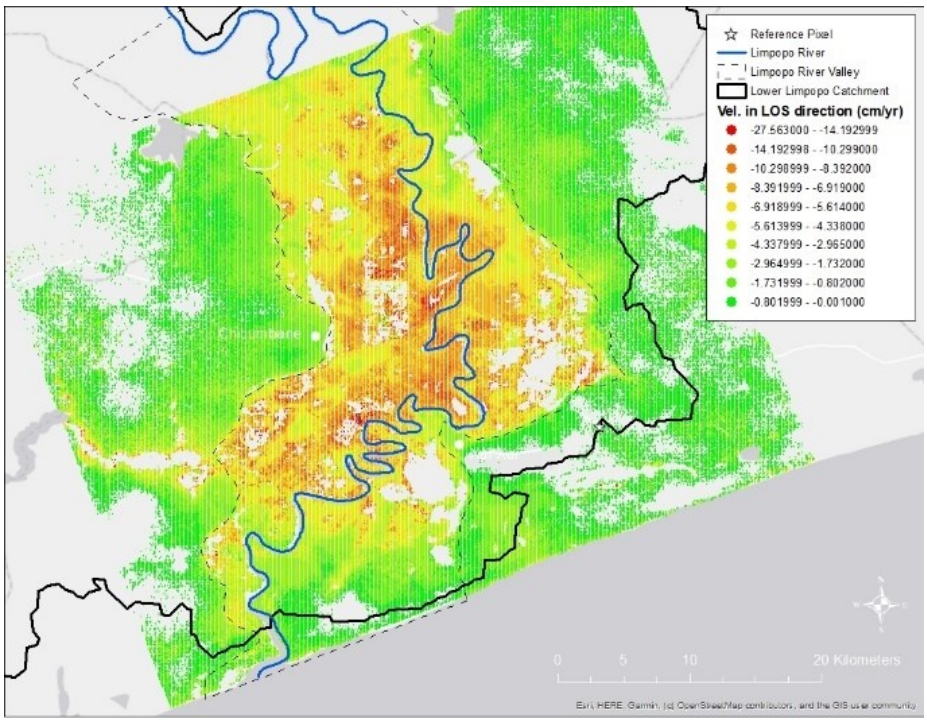

Figure 26: Subsidence results of the 2021 dry season. Uplifted pixels are not shown.

Histograms were created for each dry season to show the distribution of velocity rates in the Limpopo River Valley (Figures 27, 29, 31, 33 and 35). Velocity values greater than 0 indicate uplifted pixels while values less than 0 indicate subsided pixels. All five histograms indicate that subsidence is more prevalent than uplift in the Limpopo River valley during the dry season. It should be noted that all velocity measurements are in the line-of-site (LOS) direction, which corresponds to the angle that the satellite took the image at. LOS measurements contain contributions from both horizontal and vertical movement.

Mean and median velocities within the distribution are indicated by the pink and blue bars, respectively. Highest subsidence rates were observed during the 2021 dry season with a mean velocity of -5.406 cm/yr and median velocity of -5.481 cm/yr. Lowest subsidence rates were observed during the 2018 dry season with a mean velocity of -1.896 cm/yr and median velocity of -2.032 cm/yr. By averaging all of the mean dry season subsidence rates, we can estimate the average rate of movement in the lower Limpopo River valley to be -2.980 cm/yr.

Velocity rates within the Limpopo River Valley were also represented spatially in Figures 28, 30, 32, 34 and 36. Much like Figures 22-26, uplifted pixels were removed for the sake of visualization. Many of the rapidly subsiding areas within the river valley are in the location of agricultural schemes, particularly in the area due north of the Xai-Xai District. Subsidence at this agricultural scheme can be easily observed in Figure 30 and 32. Without additional data regarding wet season land deformation, groundwater levels or conductivity measurements, it is difficult to establish causation for the observed dry season subsidence of the river valley. However, the concentration of high subsidence in agricultural areas raises concerns about potential over-extraction of groundwater for irrigation.

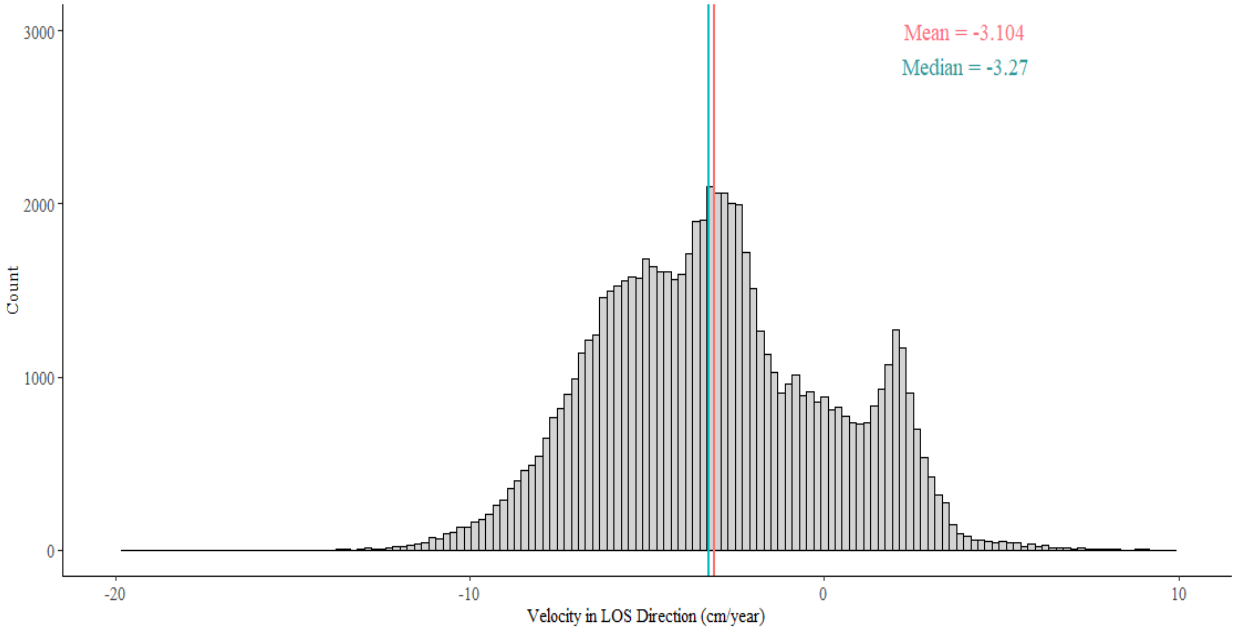

Figure 27: Distribution of velocity values in the lower Limpopo River valley during the 2017 dry season where values > 0 represent uplift and values < 0 represent subsidence.

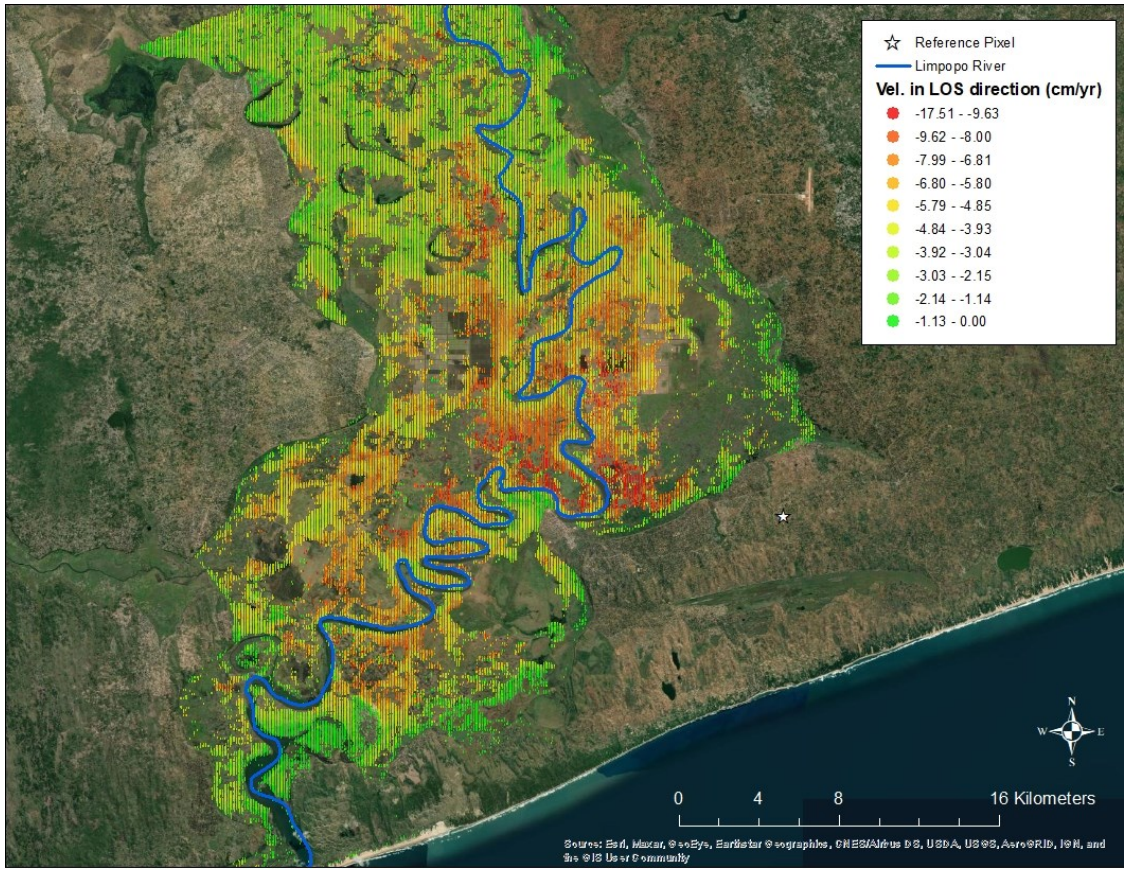

Figure 28: Subsidence of the Limpopo River valley during the 2017 dry season with uplifted pixels excluded.

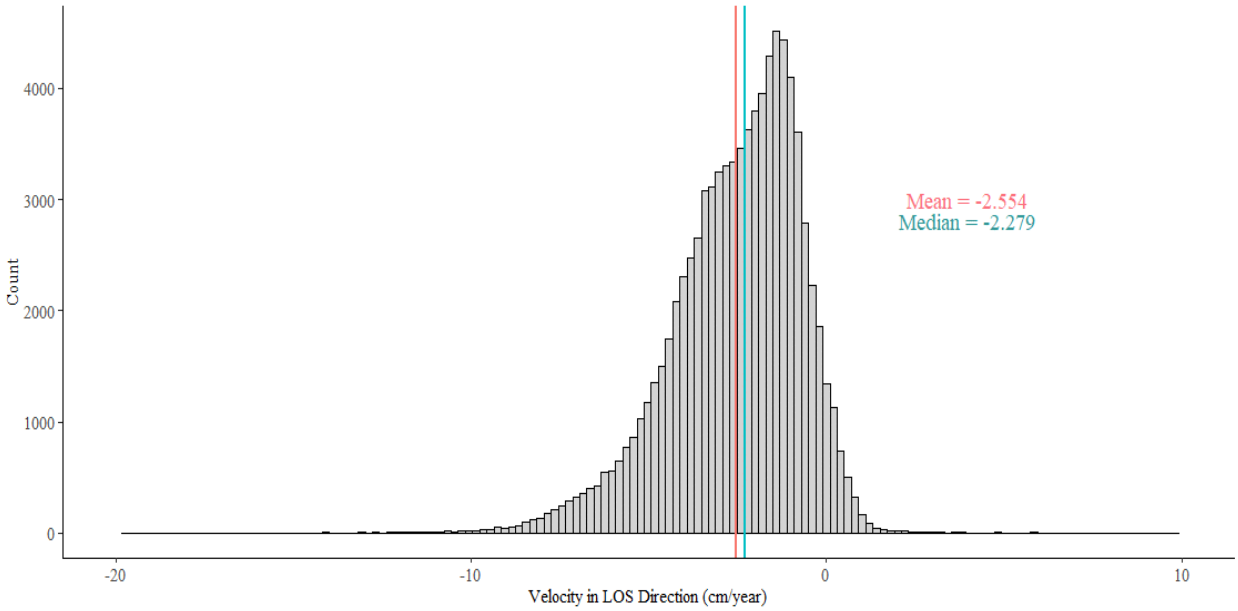

Figure 29: Distribution of velocity values in the lower Limpopo River valley during the 2018 dry season where values > 0 represent uplift and values < 0 represent subsidence.

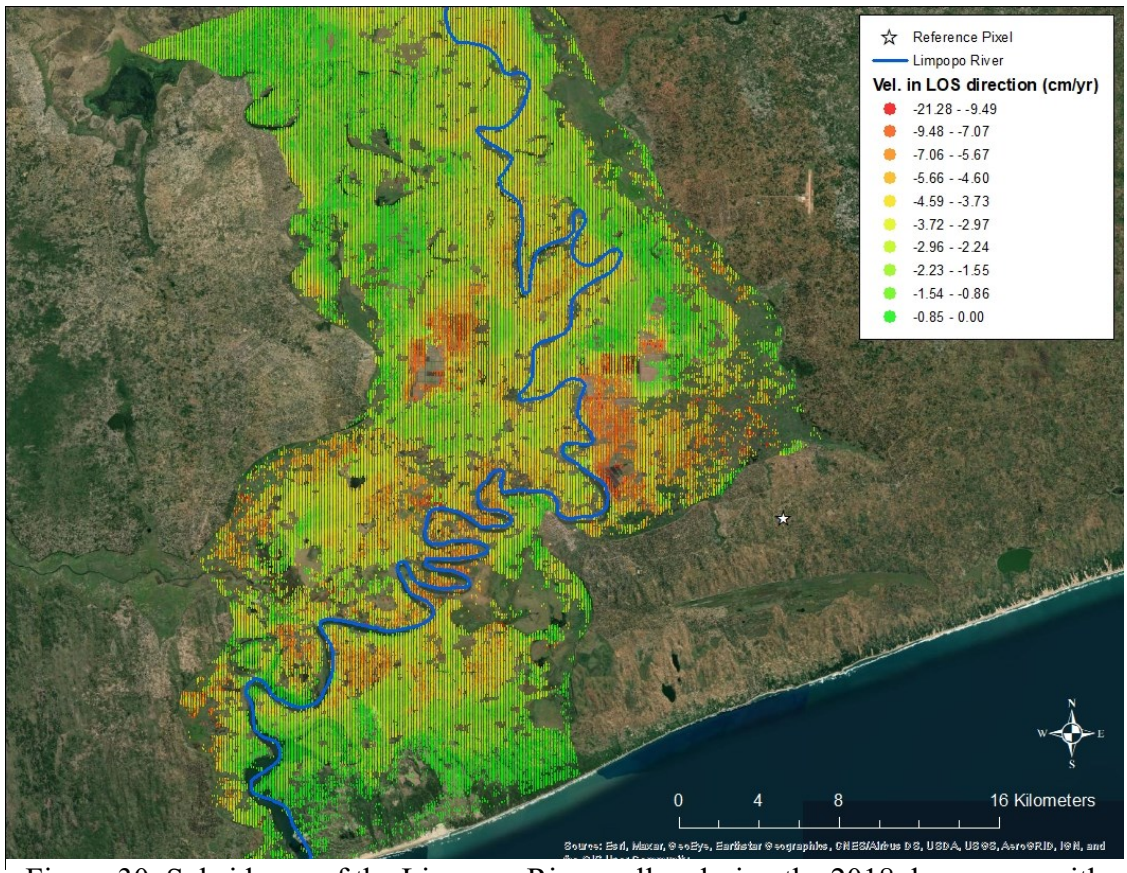

Figure 30: Subsidence of the Limpopo River valley during the 2018 dry season with uplifted pixels excluded.

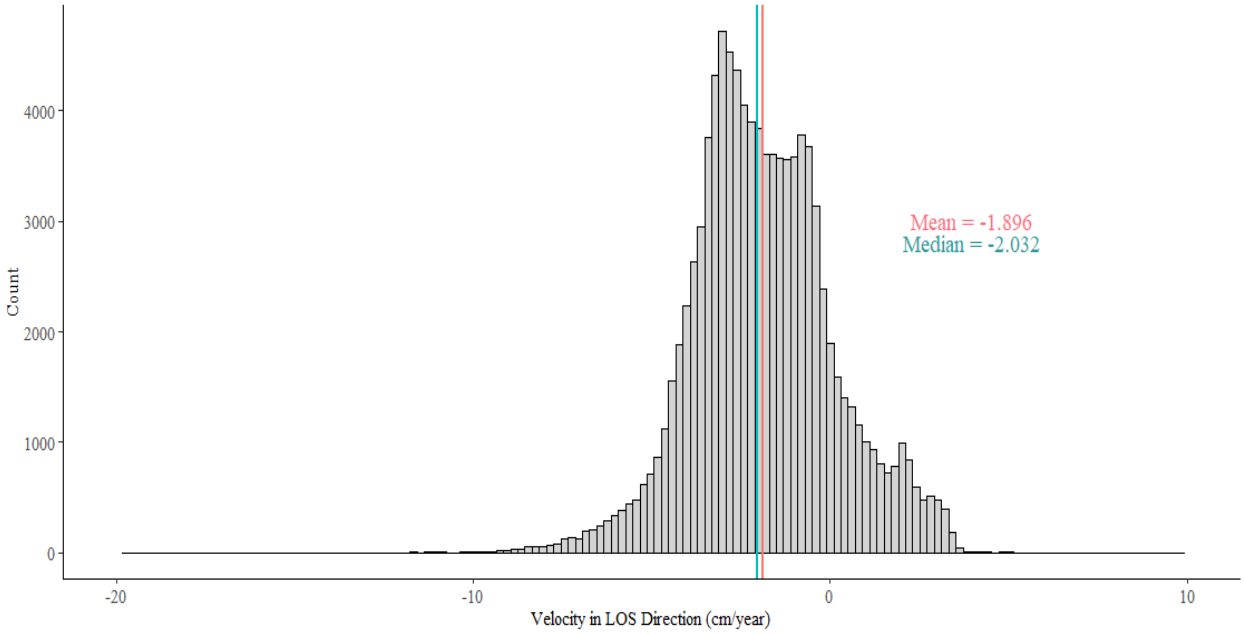

Figure 31: Distribution of velocity values in the lower Limpopo River valley during the 2019 dry season where values > 0 represent uplift and values < 0 represent subsidence.

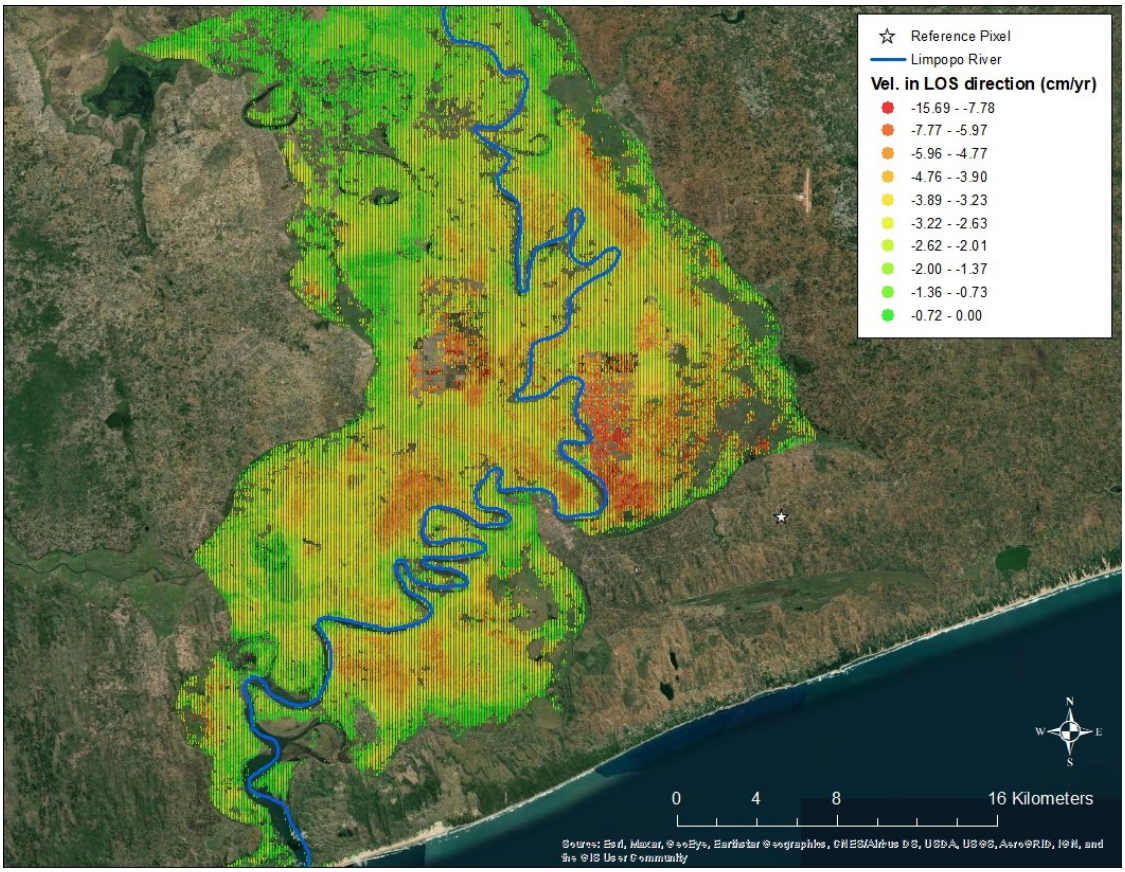

Figure 32: Subsidence of the Limpopo River valley during the 2019 dry season with uplifted pixels excluded.

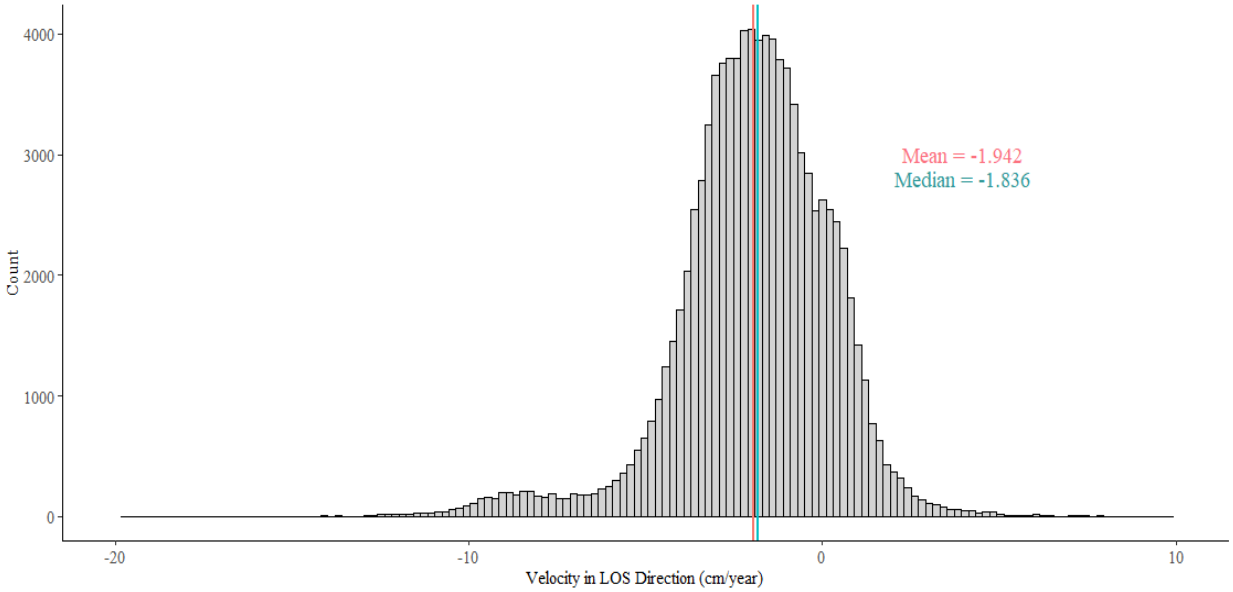

Figure 33: Distribution of velocity values in the lower Limpopo River valley during the 2020 dry season where values > 0 represent uplift and values < 0 represent subsidence.

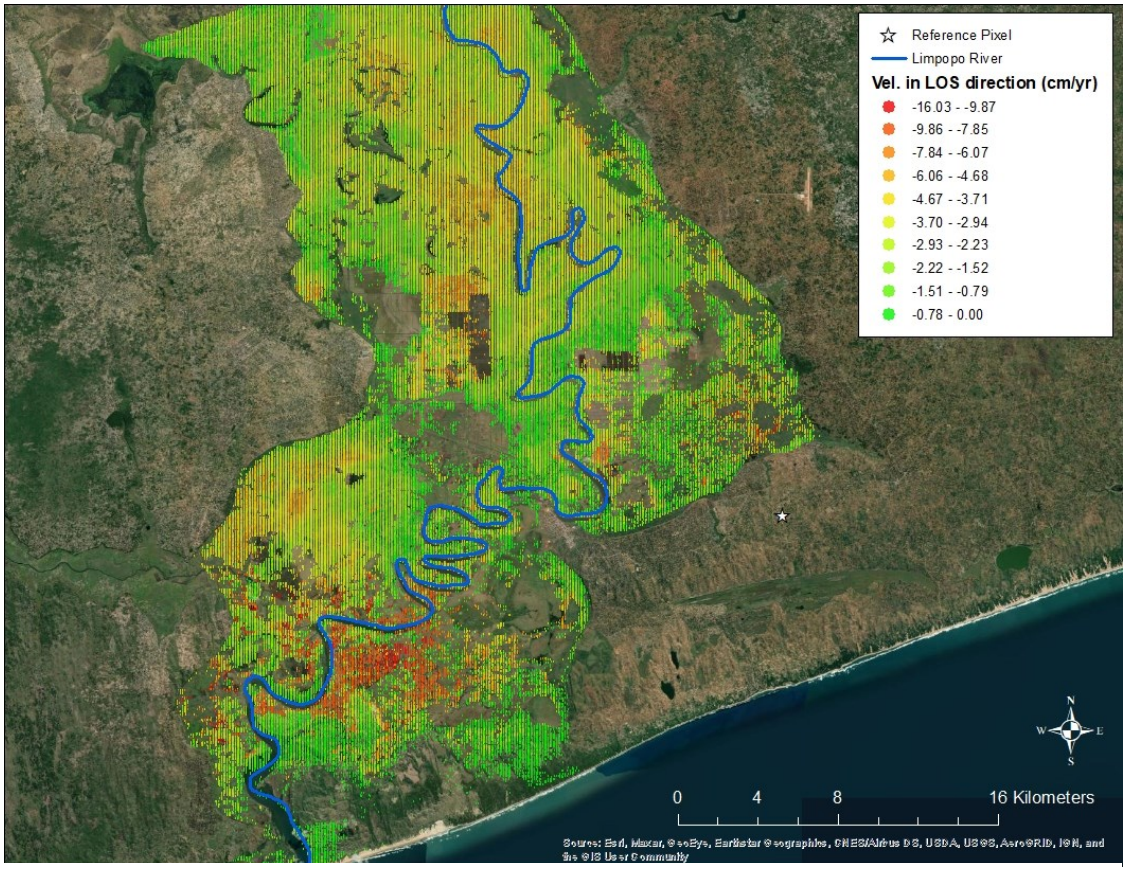

Figure 34: Subsidence of the Limpopo River valley during the 2020 dry season with uplifted pixels excluded.

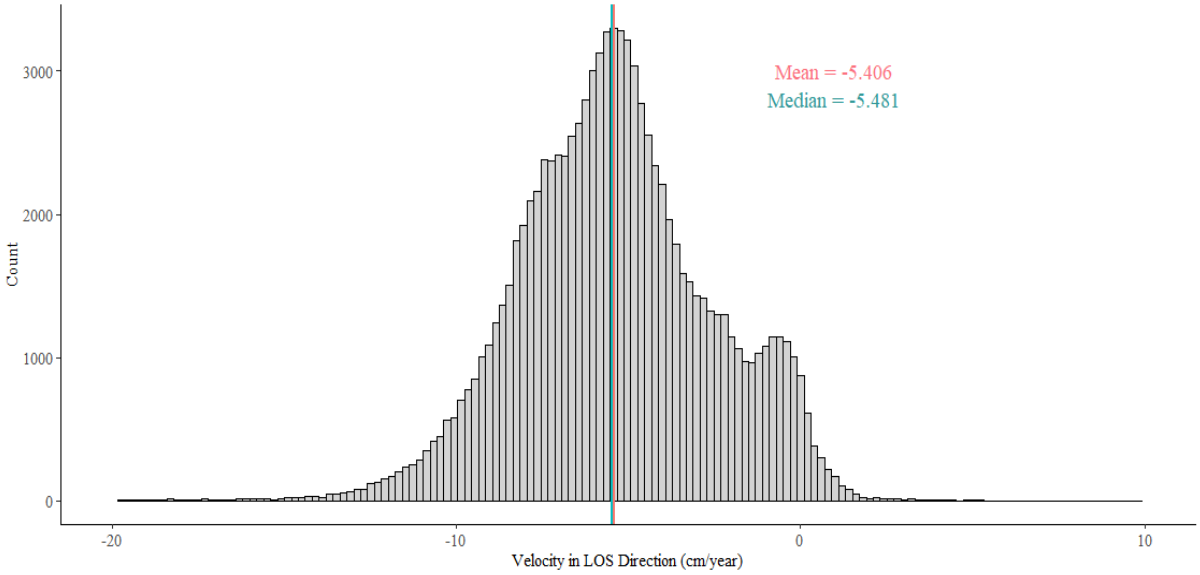

Figure 35: Distribution of velocity values in the lower Limpopo River valley during the 2021 dry season where values > 0 represent uplift and values < 0 represent subsidence.

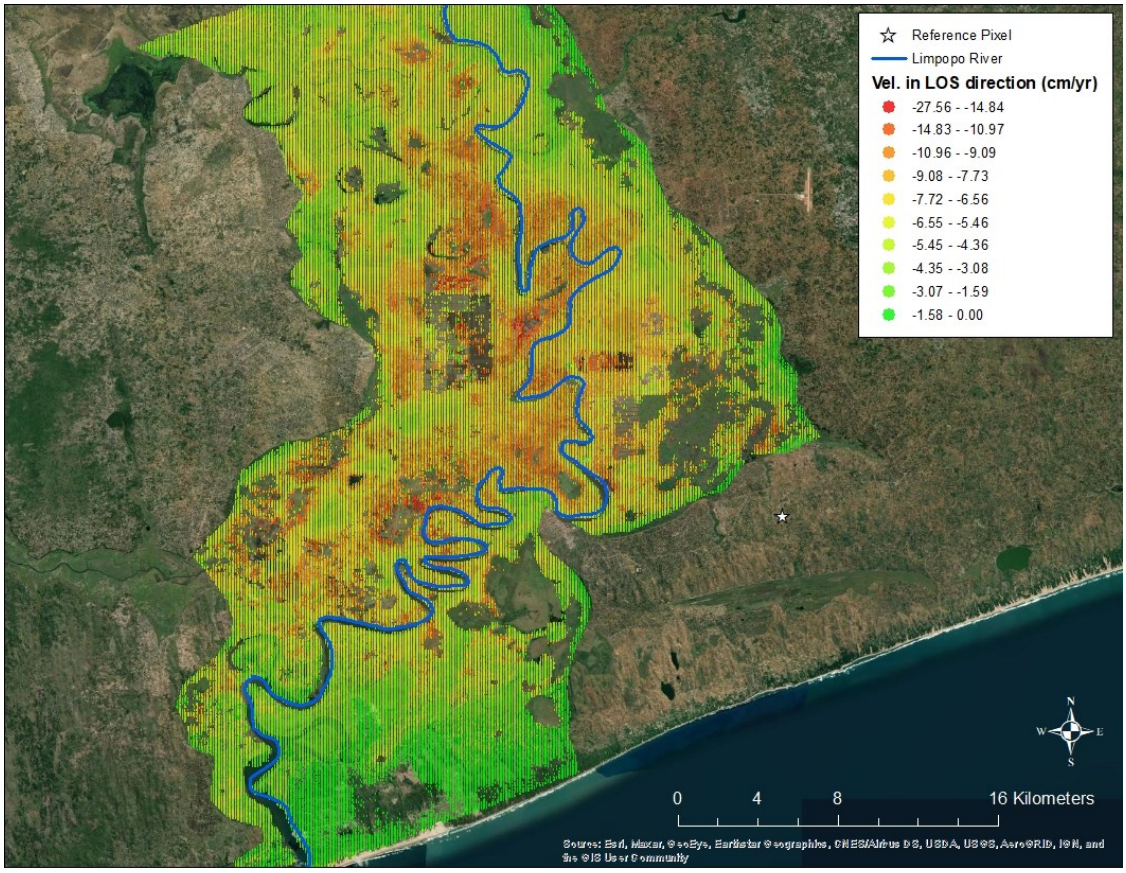

Figure 36: Subsidence of the Limpopo River valley during the 2021 dry season with uplifted pixels excluded.

3.2 RIVER HEIGHT AND SEA LEVEL

Assessment of variations in river height for the hydrometric gauges at Chokwe (E-35) and Xai-Xai (E-38) in the Limpopo River revealed decreasing water levels at both locations over time. The Chokwe gauge, situated just south of the Macarretane Weir, recorded height variations at an average of -6.44 cm/yr (Figure 37). Farther downstream, near the mouth of the Limpopo, the gauge at Xai-Xai recorded height reductions variations at a rate of -1.93 cm/yr (Figure 38). It is likely that, because both gauges are recording height reductions, water availability in the LLRB is being negatively impacted by upstream use.

Loss of water height can potentially have devastating impacts on water quality in the LLRB. Flow reductions could mean that less sediment is being transported to the lower Limpopo Basin, which could be a potential cause for the observed subsidence. Along with sediment depravation and water shortages, reduced freshwater flow in the seaward direction can lessen hydraulic pressure in the estuary, allowing saltwater intrusion to travel farther upstream. This upstream movement could potentially contaminate groundwater wells and make freshwater sources unusable for crop irrigation – a process which would be detrimental to the agricultural operations at Xai-Xai and Chokwe. However, without continuously operating conductivity sensors we do have enough data available to compare temporal trends in river height with changes in salinity levels over time.

Daily measurements of water height at the Durban, South Africa tide gauge reveal a gradual increase in average eustatic sea level rise at a rate of 0.114 cm/yr (Figure 39). Our analysis assumes that the rate of eustatic sea level rise at Durban is similar at Xai-Xai. This rate of sea-level rise, though small, can still exacerbate flood risk and saltwater contamination during storm surges and tropical cyclone events.

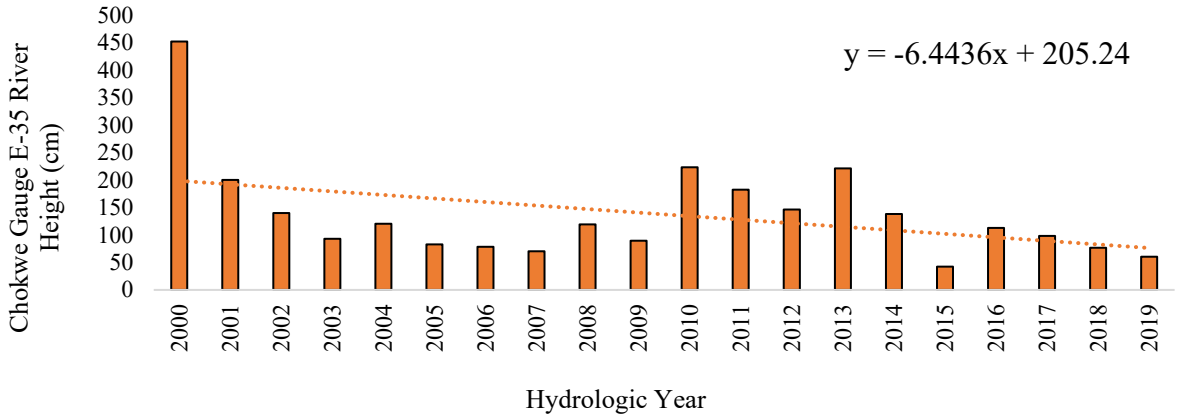

Figure 39: Annual mean river height from hydrometric gauge E-35 at Chokwe, Mozambique.

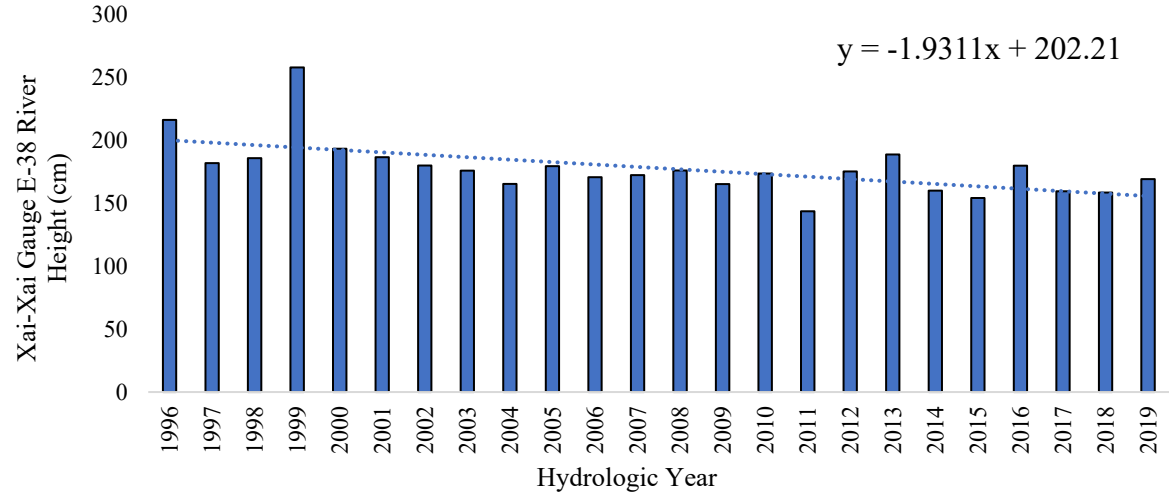

Figure 38: Annual mean river height from hydrometric gauge E-38 at Xai-Xai, Mozambique.

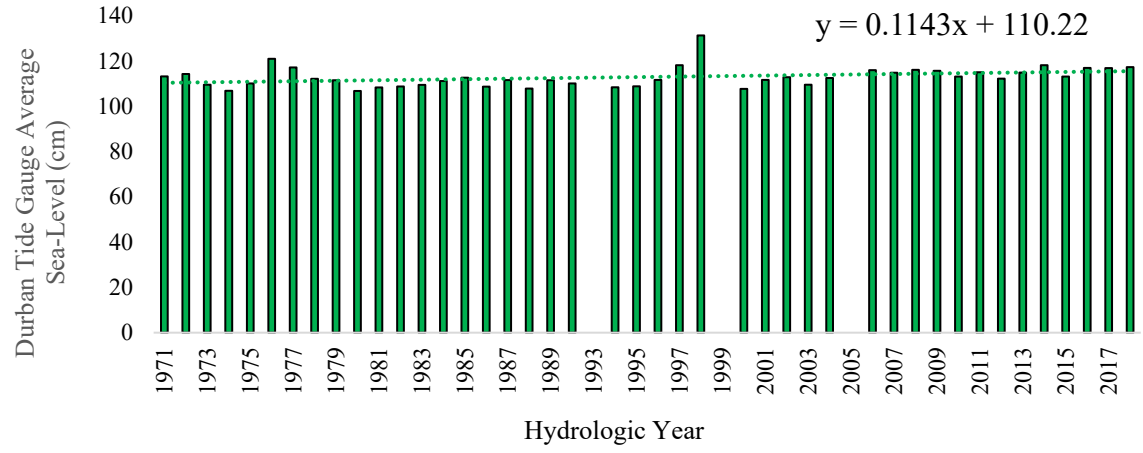

Figure 37: Annual mean sea height from tide gauge at Durban, South Africa.

CHAPTER 4: CONCLUSIONS

In the lower Limpopo River Basin in southern Mozambique, reports of increased salinization of water resources during the dry season, as well as geophysical characteristics of the subsurface and groundwater use suggest that land subsidence could potentially be occurring in the area. In Section 1.5, we outlined our research objectives to be 1) determine if land subsidence is occurring in the lower Limpopo River Basin and 2) assess the potential contribution of subsidence to reports of saltwater intrusion. We hypothesized that land subsidence is occurring within the lower Limpopo River Basin at a rate that, when combined with sea level rise and river height changes, is contributing to increased saltwater intrusion upstream in the Limpopo River.

Sentinel-1 interferometric synthetic aperture radar (InSAR) was used to detect potential land subsidence during the dry seasons (May to October) of 2017 to 2021. Subsidence results were combined with measurements of eustatic sea-level rise, recorded by the Durban, South Africa tide gauge, and height of Limpopo River at Xai-Xai, to assess the potential risk of saltwater intrusion into the Limpopo River. Results of this analysis indicate that subsidence has occurred within the lower Limpopo River Valley in each of the studied dry seasons at a mean rate of -2.98 cm/yr. Eustatic sea-level rise was measured at 0.114 cm/yr, and river height at the Xai-Xai gauge was measured at –1.93 cm/yr. Land subsidence has the highest rate of change compared to the two other factors and therefore, rates of relative sea level rise are greater than eustatic sea level rise measurements (Figure 40). The decrease of land and river height decreases hydrostatic pressure on the freshwater side of the estuary, allowing for gradual salinization and upstream movement of the intrusion over time. Therefore, our hypothesis is supported that land subsidence is occurring in the LLRB and likely contributing to reports of saltwater intrusion, at least during the dry season.

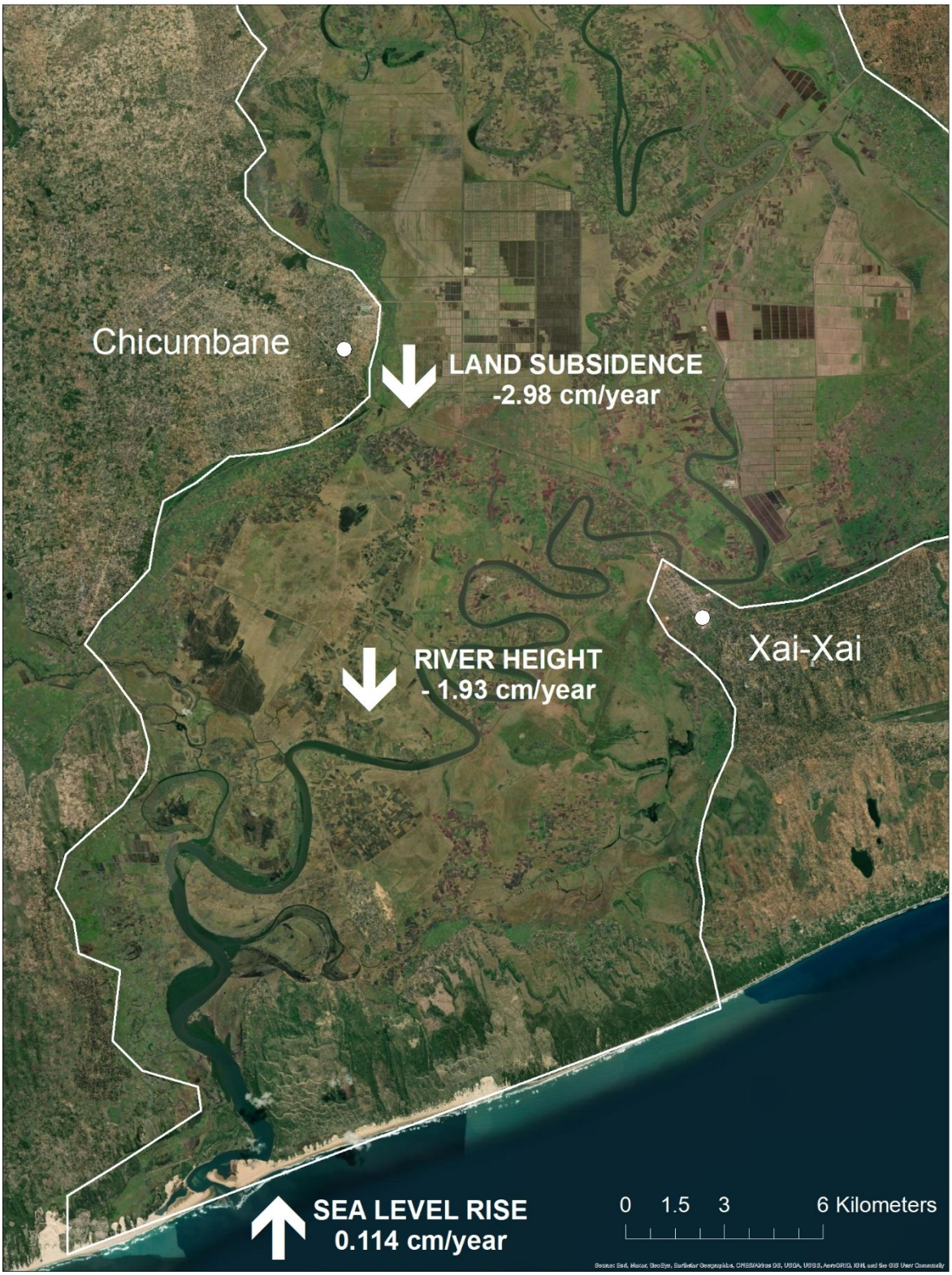

Figure 40: Assessment of saltwater intrusion potential based on rates of sea-level rise, river height reductions and land subsidence in the lower Limpopo River valley.

4.1 LIMITATIONS AND FUTURE WORK

4.1.1 INSAR METHODOLOGY

One of the major limitations of this study is the inability to monitor subsidence throughout the region's wet season (November to April). Even with the implementation of a tropospheric delay model, interferograms generated from dates of the wet season experienced significant decorrelation across the study area. Low coherence is indicative of poor backscattered signals, meaning that the data from low coherence interferograms in unreliable. The cause of wet season decorrelation in the LLRB is not known. In recent years, there have been multiple studies published that investigate the relationship between soil moisture and interferometric phase (Nolan & Fatland, 2003; Barrett, Whelan & Dwyer, 2013; Eshqi Molan & Lu, 2020). It is possible that decorrelation during the wet season is due to ground saturation, which can cause scattering, creating noisy interferograms. It is also possible that the tropospheric delay model used in this study does not accurately model the phase contribution from extreme precipitation events that are experience during monsoonal events in the LLRB.

Without including the wet season images in the SBAS interferometric network, it is difficult to assess long-term subsidence trends. While the results are reported in cm/yr, the deformation has only been observed during the dry season. However, it is possible that aquifers undergo dry season compaction with the possibility of wet season expansion. from increased water withdrawal rates and limited recharge during the dry season and subsequent high recharge during the wet season. It is important to understand the elasticity and recharge of aquifers in the LLRB, as continuous subsidence can eventually lead to permanent pore closure and loss of aquifer storage capacity. This would be determinantal to those that rely on groundwater as a primary source of freshwater in coastal communities.

To gain an understanding of wet season deformation trends, we recommend using an alternative subsidence monitoring technique. Specifically, we believe the installation of a series of GNSS beacons, both in and out of the Limpopo River valley, would not only better track wet season changes, but the data can also be used to improve and validate studies such as this. For example, GNSS beacons can be used to verify stable reference pixel locations for InSAR analysis.

Another limitation to InSAR methodology is the calculation of velocity in the line-of-site (LOS) direction. Measurements in the LOS direction show if ground level is moving toward or away from the satellite. However, because the SAR images are taken from an angle, these measurements do not necessarily indicate vertical subsidence or uplift. There are methods for deriving the vertical and horizontal components of LOS measurements, however, this procedure is outside the scope of this study and was not applied to our data.

4.1.2 DATA AVAILABILITY

The lack of available groundwater data in the LLRB hinders our ability to establish a cause for the observed dry season subsidence. Much of the subsidence is concentrated in agricultural areas within the floodplain. This could indicate that these agricultural operations are pumping groundwater for irrigation, resulting in aquifer compaction. Many studies of groundwater related subsidence use well measurements, specifically of hydraulic head, to establish correlation between rates of subsidence and rates of extraction. However, groundwater levels are not recorded in the LLRB, and even the location of wells, particularly those for small hold farms and domestic purposes, are not well documented. To better understand the impact that groundwater extraction may be having on land subsidence and saltwater intrusion in the LLRB,

we recommend the establishment of a groundwater monitoring network in the Limpopo River valley.

A lack of water quality data is also a limiting factor to this study. Although our results do indicate that subsidence is likely contributing to the reported saltwater intrusion in the LLRB during the dry season, temporal and spatial conductivity data for surface and groundwater sources are scarce. It is also possible that subsidence in the basin could be influenced by reduced sediment aggradation from upstream dams. Measurements of water height indicate that the LLRB is losing water at both gauges over time. Decreased river flow can limit erosion, which in turn, reduces sediment supply to the lower Limpopo. However, without time-series data of total suspended sediment in the lower Limpopo River, it is difficult to draw a connection between sediment deposition and subsidence. However, there are active plans to install conductivity sensors in the lower Limpopo River to better understand the spatial and temporal trends of saltwater intrusion.

Finally, it could be useful to conduct an extensive soil sampling of the study area to help determine the cause of the observed subsidence. Soils that are rich in clay and silt, known as cohesive soils, shrink expand when they are wet and sink when they are dry. Aquitards that are composed of clay are at high risk to experience subsidence when coupled with groundwater extraction. By understanding the composition of the alluvium throughout the floodplain, spatial patterns may be established between areas of high subsidence and concentrations of clay and silt.

Land subsidence has been successfully mitigated in other places throughout the world with groundwater regulation and artificial injection (Sato, Haga & Nishino, 2006; Gambolati & Teatini, 2015). In the deltaic Asian megacities of Jakarta, Tokyo, Manila, and Ho Chi Minh City adaptations such as raised floors walking paths and the installation of seawalls and other

hydrologic infrastructure have been used to combat the effects of coastal land subsidence (Cao et al., 2021). However, in the LLRB it is difficult to determine a mitigation or adaptation technique without a better understanding of the cause of observed dry season subsidence. Therefore, improving data collection is the first step to effective subsidence management and protection of coastal communities in the LLRB.

CHAPTER 5: REFERENCES

Abidin, H. Z., Andreas, H., Gumilar, I., Sidiq, T., & Gamal, M. (2015). *Environmental Impacts of Land Subsidence in Urban Areas of Indonesia*.

Antonellini, M., Mollema, P., Giambastiani, B., Bishop, K., Caruso, L., Minchio, A., Pellegrini, L., Sabia, M., Ulazzi, E., & Giovanni, G. (2008). Salt water intrusion in the coastal aquifer of the southern Po Plain, Italy. *Hydrogeology Journal*, *16*, 1541–1556. https://doi.org/10.1007/s10040-008-0319-9

Ashton, P. & Hardwick, D. (2008). *Key Challenges Facing Water Resource Management in South Africa* [Conference Presentation]. 2nd Biennial CSIR Conference, Pretoria, South Africa.

Bagheri-Gavkosh, M., Hosseini, S. M., Ataie-Ashtiani, B., Sohani, Y., Ebrahimian, H., Morovat, F., & Ashrafi, S. (2021). Land subsidence: A global challenge. *Science of The Total Environment*, *778*, 146193. https://doi.org/10.1016/j.scitotenv.2021.146193

Barrett, B., Whelan, P., & Dwyer, E. (2013). Detecting changes in surface soil moisture content using differential SAR interferometry. *International Journal of Remote Sensing*, *34*(20), 7091–7112. https://doi.org/10.1080/01431161.2013.813654

Becker, R. H., & Sultan, M. (2009). Land subsidence in the Nile Delta: Inferences from radar interferometry. *The Holocene*, *19*(6), 949–954. https://doi.org/10.1177/0959683609336558

Bell, J. W., Amelung, F., Ferretti, A., Bianchi, M., & Novali, F. (2008). Permanent scatterer InSAR reveals seasonal and long-term aquifer-system response to groundwater pumping and artificial recharge. *Water Resources Research*, *44*(2). https://doi.org/10.1029/2007WR006152

Berardino, P., Fornaro, G., Lanari, R., & Sansosti, E. (2002). A new algorithm for surface deformation monitoring based on small baseline differential SAR interferograms. *IEEE Transactions on Geoscience and Remote Sensing*, *40*(11), 2375–2383. https://doi.org/10.1109/TGRS.2002.803792

Cao, A., Esteban, M., Valenzuela, V. P. B., Onuki, M., Takagi, H., Thao, N. D., & Tsuchiya, N. (2021). Future of Asian Deltaic Megacities under sea level rise and land subsidence: Current adaptation pathways for Tokyo, Jakarta, Manila, and Ho Chi Minh City. *Current Opinion in Environmental Sustainability*, *50*, 87–97. https://doi.org/10.1016/j.cosust.2021.02.010

Crosetto, M., Monserrat, O., Cuevas-González, M., Devanthéry, N., & Crippa, B. (2015). Persistent Scatterer Interferometry: A review. *ISPRS Journal of Photogrammetry and Remote Sensing*. https://doi.org/10.1016/j.isprsjprs.2015.10.011

Edmonds, D. A., Caldwell, R. L., Brondizio, E. S., & Siani, S. M. O. (2020). Coastal flooding will disproportionately impact people on river deltas. *Nature Communications*, *11*(1), 4741. https://doi.org/10.1038/s41467-020-18531-4

Erkens, G., Bucx, T., Dam, R., de Lange, G., & Lambert, J. (2015). Sinking coastal cities. *Proceedings of the International Association of Hydrological Sciences*, *372*, 189–198. https://doi.org/10.5194/piahs-372-189-2015

Eshqi Molan, Y., & Lu, Z. (2020). Can InSAR Coherence and Closure Phase Be Used to Estimate Soil Moisture Changes? *Remote Sensing*, *12*, 1511. https://doi.org/10.3390/rs12091511

Food and Agriculture Organization (FAO) of the United Nations. (2004). Drought Impact, Mitigation and Prevention in the Limpopo River Basin. Retrieved from https://www.fao.org/3/y5744e/y5744e00.htm

Food and Agriculture Organization (FAO) of the United Nations. (2005). Irrigation in Africa in figures: AQUASTAT survey.

Galloway, D. L., & Burbey, T. J. (2011). Review: Regional land subsidence accompanying groundwater extraction. In *Hydrogeology Journal* (Vol. 19, Issue 8, p. 14591486). https://doi.org/10.1007/s10040-011-0775-5

Galloway, D. L., Erkens, G., Kuniansky, E. L., & Rowland, J. C. (2016). Preface: Land subsidence processes. *Hydrogeology Journal*, *24*(3), 547–550. https://doi.org/10.1007/s10040-016-1386-y

Galloway, D. L., Hudnut, K. W., Ingebritsen, S. E., Phillips, S. P., Peltzer, G., Rogez, F., & Rosen, P. A. (1998). Detection of aquifer system compaction and land subsidence using interferometric synthetic aperture radar, Antelope Valley, Mojave Desert, California. *Water Resources Research*, *34*(10), 2573–2585. https://doi.org/10.1029/98WR01285

Gambolati, G., Putti, M., Teatini, P., & Gasparetto Stori, G. (2006). Subsidence due to peat oxidation and impact on drainage infrastructures in a farmland catchment south of the Venice Lagoon. *Environmental Geology*, *49*(6), 814–820. https://doi.org/10.1007/s00254-006-0176-6

Gambolati, G., & Teatini, P. (2015). Geomechanics of subsurface water withdrawal and injection. *Water Resources Research*, *51*, 3922–3955. https://doi.org/10.1002/2014WR016841

Haghshenas Haghighi, M., & Motagh, M. (2019). Ground surface response to continuous compaction of aquifer system in Tehran, Iran: Results from a long-term multi-sensor InSAR analysis. *Remote Sensing of Environment*, *221*, 534–550. https://doi.org/10.1016/j.rse.2018.11.003

He, W., Zhang, J., Yu, X., Chen, S., & Luo, J. (2018). Effect of Runoff Variability and Sea Level on Saltwater Intrusion: A Case Study of Nandu River Estuary, China. *Water Resources Research*, *54*(12), 9919–9934. https://doi.org/10.1029/2018WR023285

Herrera-García, G., Ezquerro, P., Tomás, R., Béjar-Pizarro, M., López-Vinielles, J., Rossi, M., Mateos, R. M., Carreon-Freyre, D., Lambert, J., Teatini, P., Cabral-Cano, E., Erkens, G., Galloway, D., Hung, W., Kakar, N., Sneed, M., Tosi, L., Wang, H., & Ye, S. (2020). Mapping the global threat of land subsidence. *Science*. https://doi.org/10.1126/science.abb8549

Higgins, S. (2015). Review: Advances in delta-subsidence research using satellite methods. *Hydrogeology Journal*, *24*. https://doi.org/10.1007/s10040-015-1330-6

Hoekstra, A. Y., Mekonnen, M. M., Chapagain, A. K., Mathews, R. E., & Richter, B. D. (2012). Global Monthly Water Scarcity: Blue Water Footprints versus Blue Water Availability. *PLoS ONE*, *7*(2), e32688. https://doi.org/10.1371/journal.pone.0032688

Hooper, A., Segall, P., & Zebker, H. (2007). Persistent scatterer interferometric synthetic aperture radar for crustal deformation analysis, with application to Volcán Alcedo, Galápagos. *Journal of Geophysical Research*, *112*(B7), B07407. https://doi.org/10.1029/2006JB004763

Hoyt, A. M., Chaussard, E., Seppalainen, S. S., & Harvey, C. F. (2020). Widespread subsidence and carbon emissions across Southeast Asian peatlands. *Nature Geoscience*, *13*(6), 435–440. https://doi.org/10.1038/s41561-020-0575-4

Ge, L., Rizos, C., Han, S., & Zebker, H. (2001). *Mining subsidence monitoring using the combined InSAR and GPS approach*.

InSAR Principles: Guidelines for SAR Interferometry Processing and Interpretation. (2007). *European Space Agency (ESA).* Retrieved from https://www.esa.int/esapub/tm/tm19/TM-19_ptA.pdf

Ismael, F., Mbanze, A. A., Ndayiragije, A., & Fangueiro, D. (2021). Understanding the Dynamic of Rice Farming Systems in Southern Mozambique to Improve Production and Benefits to Smallholders. *Agronomy*, *11*(5), 1018. https://doi.org/10.3390/agronomy11051018

Jansing, D. E. (2021). Introduction to Synthetic Aperture Radar: Concepts and Practice (1st ed.). McGraw Hill.

Jolivet, R., Grandin, R., Lasserre, C., Doin, M.-P., & Peltzer, G. (2011). Systematic InSAR tropospheric phase delay corrections from global meteorological reanalysis data. *Geophysical Research Letters*, *38*(17). https://doi.org/10.1029/2011GL048757

Jónsson, S., Zebker, H., Segall, P., & Amelung, F. (2002). Fault Slip Distribution of the 1999 Mw 7.1 Hector Mine, California, Earthquake, Estimated from Satellite Radar and GPS Measurements. *Bulletin of the Seismological Society of America*, *92*(4), 1377–1389. https://doi.org/10.1785/0120000922

Klees, R., & Massonnet, D. (1998). Deformation measurements using SAR interferometry: Potential and limitations. *Geologie En Mijnbouw*, *77*(2), 161–176. https://doi.org/10.1023/A:1003594502801

Kondolf, G. M., Rubin, Z. K., & Minear, J. T. (2014). Dams on the Mekong: Cumulative sediment starvation. *Water Resources Research*, *50*(6), 5158–5169. https://doi.org/10.1002/2013WR014651

Li, M.-G., Chen, J.-J., Xu, Y.-S., Tong, D.-G., Cao, W.-W., & Shi, Y.-J. (2021). Effects of groundwater exploitation and recharge on land subsidence and infrastructure settlement patterns in Shanghai. *Engineering Geology*, *282*, 105995. https://doi.org/10.1016/j.enggeo.2021.105995

Liu, Z., Liu, P.-W., Massoud, E., Farr, T. G., Lundgren, P., & Famiglietti, J. S. (2019). Monitoring Groundwater Change in California's Central Valley Using Sentinel-1 and GRACE Observations. *Geosciences*, *9*(10), 436. https://doi.org/10.3390/geosciences9100436

Limpopo Basin Permanent Technical Committee (LBPTC). (2010). Joint Limpopo River Basin Study Scoping Phase Final Report. Retrieved from http://www.limpopo.riverawarenesskit.org/LIMPOPORAK_COM/_SYSTEM/DMSSTORAGE/3451EN/LIMCOM2010_SCOPINGSTUDY_ENG.PDF

Limpopo Watercourse Commission (LIMCOM). (2016). Limpopo River Basin Disaster Preparedness Action Plan. Retrieved from https://pdf.usaid.gov/pdf_docs/PA00N2HM.pdf

Limpopo Watercourse Commission (LIMCOM). (2013). Limpopo River Basin Monograph LRBMS-81137945 Final Report. Retrieved from https://dsc.duq.edu/cgi/viewcontent.cgi?article=1011&context=limpopo-policy

Loáiciga, H. A., Pingel, T. J., & Garcia, E. S. (2012). Sea Water Intrusion by Sea-Level Rise: Scenarios for the 21st Century. *Groundwater*, *50*(1), 37–47. https://doi.org/10.1111/j.1745-6584.2011.00800.x

Mosase, E., & Ahiablame, L. (2018). Rainfall and Temperature in the Limpopo River Basin, Southern Africa: Means, Variations, and Trends from 1979 to 2013. *Water*, *10*(4), 364. https://doi.org/10.3390/w10040364

Nhassengo, O. S. Z., Somura, H., & Wolfe, J. (2021). Environmental flow sustainability in the Lower Limpopo River Basin, Mozambique. *Journal of Hydrology: Regional Studies*, *36*, 100843. https://doi.org/10.1016/j.ejrh.2021.100843

Nolan, M., & Fatland, D. R. (2003). Penetration depth as a DInSAR observable and proxy for soil moisture. *IEEE Transactions on Geoscience and Remote Sensing*, *41*(3), 532–537. https://doi.org/10.1109/TGRS.2003.809931

Osmanoğlu, B., Sunar, F., Wdowinski, S., & Cabral-Cano, E. (2016). Time series analysis of InSAR data: Methods and trends. *ISPRS Journal of Photogrammetry and Remote Sensing*, *115*, 90–102. https://doi.org/10.1016/j.isprsjprs.2015.10.003

Parsons, T. (2021). The Weight of Cities: Urbanization Effects on Earth's Subsurface. *AGU Advances*, *2*(1), e2020AV000277. https://doi.org/10.1029/2020AV000277

Petrie, B., Chapman, A., Midgley, A., & Parker, R. (2015). Risk, Vulnerability & Resilience in the Limpopo River Basin – A Synthesis. Retrieved from https://www.climatelinks.org/sites/default/files/asset/document/Risk%2C%20Vulnerability%20and%20Resilience%20in%20the%20Limpopo%20River%20Basin%20-%20A%20Synthesis_0.pdf

Rogers, A. E., & Ingalls, R. P. (1969). Venus: Mapping the surface reflectivity by radar interferometry. *Science (New York, N.Y.)*, *165*(3895), 797–799. https://doi.org/10.1126/science.165.3895.797

Sato, C., Haga, M., & Nishino, J. (2006). Land Subsidence and Groundwater Management in Tokyo. *International Review for Environmental Strategies.* 6(2), 403-424. https://www.iges.or.jp/en/publication_documents/pub/peer/en/1208/IRES_Vol.6-2_403.pdf

Schlögel, R., Doubre, C., Malet, J.-P., & Masson, F. (2015). Landslide deformation monitoring with ALOS/PALSAR imagery: A D-InSAR geomorphological interpretation method. *Geomorphology*, *231*, 314–330. https://doi.org/10.1016/j.geomorph.2014.11.031

Schmidt, C. W. (2015). Delta Subsidence: An Imminent Threat to Coastal Populations. *Environmental Health Perspectives*, *123*(8), A204–A209. https://doi.org/10.1289/ehp.123-A204

Sharp, G., & Kahler, D. M., (2019). WaterQ2: Understanding Water Quality and Quantity in the Limpopo Basin, 2019 Stakeholder Meeting Report. Thohoyandou, South Africa: Limpopo Resilience Lab.

Stanley, D. J., & Clemente, P. L. (2014). Clay Distributions, Grain Sizes, Sediment Thicknesses, and Compaction Rates to Interpret Subsidence in Egypt's Northern Nile Delta. *Journal of Coastal Research*, *30*(1), 88–101. https://doi.org/10.2112/JCOASTRES-D-13-00146.1

Stanley, D. J., & Warne, A. G. (1994). Worldwide Initiation of Holocene Marine Deltas by Deceleration of Sea-Level Rise. *Science*, *265*(5169), 228–231. https://doi.org/10.1126/science.265.5169.228

Stanley, D. J., & Warne, A. G. (1997). Holocene Sea-Level Change and Early Human Utilization of Deltas. *GSA Today*. https://www.semanticscholar.org/paper/Holocene-Sea-Level-

Change-and-Early-Human-of-Deltas-Stanley-Warne/0e3992d363ef6333e16e043782341941529cc1c4

Syvitski, J. P. M., Vörösmarty, C. J., Kettner, A. J., & Green, P. (2005). Impact of humans on the flux of terrestrial sediment to the global coastal ocean. *Science (New York, N.Y.)*, *308*(5720), 376–380. https://doi.org/10.1126/science.1109454

Syvitski, J. P. M., Kettner, A. J., Overeem, I., Hutton, E. W. H., Hannon, M. T., Brakenridge, G. R., Day, J., Vörösmarty, C., Saito, Y., Giosan, L., & Nicholls, R. J. (2009). Sinking deltas due to human activities. *Nature Geoscience*, *2*(10), 681–686. https://doi.org/10.1038/ngeo629

Törnqvist, T. E., Wallace, D. J., Storms, J. E. A., Wallinga, J., van Dam, R. L., Blaauw, M., Derksen, M. S., Klerks, C. J. W., Meijneken, C., & Snijders, E. M. A. (2008). Mississippi Delta subsidence primarily caused by compaction of Holocene strata. *Nature Geoscience*, *1*(3), 173–176. https://doi.org/10.1038/ngeo129

United Nations, Department of Economic and Social Affairs, Population Division (2019). World Urbanization Prospects: The 2018 Revision (ST/ESA/SER.A/420). New York: United Nations.

Van der Zaag, P., Juízo, D., Vilanculos, A., Bolding, A., & Uiterweer, N. C. (2010). Does the Limpopo River Basin have sufficient water for massive irrigation development in the plains of Mozambique? *Physics and Chemistry of the Earth, Parts A/B/C*, *35*, 832–837. https://doi.org/10.1016/j.pce.2010.07.026

Wu, P., Wei, M. (Matt), & D'Hondt, S. (2022). Subsidence in Coastal Cities Throughout the World Observed by InSAR. *Geophysical Research Letters*, *49*(7). https://doi.org/10.1029/2022GL098477

Xiao, H., Tang, Y., Li, H., Zhang, L., Ngo-Duc, T., Chen, D., & Tang, Q. (2021). Saltwater intrusion into groundwater systems in the Mekong Delta and links to global change. *Advances in Climate Change Research*, *12*(3), 342–352. https://doi.org/10.1016/j.accre.2021.04.005

Yang, Q., Ke, Y., Zhang, D., Chen, B., Gong, H., Lv, M., Zhu, L., & Li, X. (2018). Multi-Scale Analysis of the Relationship between Land Subsidence and Buildings: A Case Study in an Eastern Beijing Urban Area Using the PS-InSAR Technique. *Remote Sensing*, *10*(7), 1006. https://doi.org/10.3390/rs10071006

Yunjun, Z., Fattahi, H., & Amelung, F. (2019). Small baseline InSAR time series analysis: Unwrapping error correction and noise reduction. *Computers & Geosciences*, *133*, 104331. https://doi.org/10.1016/j.cageo.2019.104331

5.1 DATA SOURCES

ASF DAAC 2021, contains modified Copernicus Sentinel data 2015-2021, processed by ESA.

Caldwell, P. C., M. A. Merrifield, P. R. Thompson (2015), Sea level measured by tide gauges from global oceans — the Joint Archive for Sea Level holdings (NCEI Accession 0019568), Version 5.5, *NOAA National Centers for Environmental Information*, Dataset, doi:10.7289/V5V40S7W.

Karra, K., Kontgis, C., Statman-Weil, Z., Mazzariello, J. C., Mathis, M., & Brumby, S. P. (2021). Global land use / land cover with Sentinel 2 and deep learning. *2021 IEEE International Geoscience and Remote Sensing Symposium IGARSS*, 4704–4707. https://doi.org/10.1109/IGARSS47720.2021.9553499

NASA Shuttle Radar Topography Mission (SRTM)(2013). Shuttle Radar Topography Mission (SRTM) Global. Distributed by OpenTopography. https://doi.org/10.5069/G9445JDF.